Quantitative mineralogy for facies definition in the Marcellus Shale (Appalachian Basin, USA) using XRD-XRF integration

Brittany N. Hupp[1] **

Joseph J. Donovan[1]

[1]Department of Geology & Geography
West Virginia University
330 Brooks Hall
Morgantown, WV, 26506-6300

**present address:
Department of Geoscience
University of Wisconsin-Madison
1215 W. Dayton St.
Madison, WI 53706-1692

** corresponding author
Email: bhupp@wisc.edu
Phone: +1 740-404-2559
FAX: 608-262-0693

March 2018

Submitted to: *Sedimentary Geology*

Document filename: Hupp and Donovan_Marcellus Mineralogy_SedGeo.doc

Competing interests statement: Neither author has any competing interests to declare.

Conflicts of interest: None.

Abstract

Determining mineralogy of mature sedimentary rocks, particularly mudstone, often defaults to qualitative or semi-quantitative methods due to difficulties in identifying multiple unknown phases. Constraining mineral abundances is particularly difficult in mudstone due to preferred mounting orientation in common phyllosilicate phases, leading to overestimation of clay minerals and mica. We introduce a workflow for a quantitative approach to constraining mineralogy within mudstone by integrating x-ray diffraction (XRD) and x-ray fluorescence (XRF) data sets collected on splits of the same samples. The technique involves partitioning XRF cation concentrations into XRD-identified silicate, carbonate, and sulfide phases, then estimating quartz by XRF SiO_2 balance. This method is applied to an example dataset from the economically-significant Marcellus Shale (Middle Devonian). Conventional reference-intensity ratio (RIR) interpretation identified nine mineral phases (quartz, muscovite, illite, pyrite, chlorite, albite, calcite, dolomite, and barite). Their abundances were then re-estimated using more highly-accurate XRF-derived elemental concentrations with stoichiometry from the identified XRD reference phases. XRF Al_2O_3 was used to corroborate the calculated XRD-XRF results, for quality control. While errors cannot be easily quantified, the resulting XRD-XRF mineralogic abundances are thought to be more accurate than RIR and to remove preferred-orientation bias induced using RIR, causing overestimation of clay minerals and mica and underestimation of quartz. Cluster analysis of the XRD-XRF results identified four mineralogical facies that provide insight into potential primary depositional controls on organic matter preservation within the Marcellus. This XRD-XRF integration method provides a general framework for estimating mineralogy quantitatively in mudstone, although dataset-specific adjustments to the method may be required for different mineralogical suites.

Keywords: clay minerals; Marcellus Shale; mineralogy; mudstone; x-ray diffraction; x-ray fluorescence

1 Introduction

Mineral identification by x-ray diffraction (XRD) may be undertaken using either qualitative (e.g., identification), semi-quantitative, or quantitative methodologies, each of which has its own applications, limitations, and pitfalls (Klug and Alexander, 1974). Simple identification can generally be accomplished with ease for single mineral phases and, with more difficulty, for mixtures of two to several phases. Sources of error in this determination include variable composition and/or structure of unknowns with respect to reference phases (Srodon et al., 2001), inadequate sample preparation (Jenkins, 1989), and unknowns occurring in low concentration within the mixture. All of these problems, and several others, are compounded in semi-quantitative and, especially, quantitative analysis of mineral composition of rocks and soils.

One application in which quantification by XRD poses a major challenge is the mineralogy of marine shale, also termed mudstone. Despite being geochemically mature, these rocks are deposited in either epicontinental or basin settings and reflect provenance of local sediment/orogenic sources as well as the effects of diagenesis and/or metamorphism (Saupe and Vegas, 1987; Potter et al., 2005; Zhou and Keeling, 2013). As a result, mineralogical suites in such strata are commonly diverse and can contain multiple phases of clay mineral, mica, carbonate, aluminosilicate, and sulfide groups, as well as quartz and organic matter. In addition to the large number of phases, an additional obstacle to quantification is preferred orientation of, especially, phyllosilicate phases. Upon mounting, some minerals tend to align according to their crystallographic orientation including gypsum (Grattin-Bellew, 1975) and, especially, clays and micas (Braun 1986; Kolka et al. 1994; da Silva et al., 2011). While various methods have been described to minimize preferred orientation (Poppe et al., 2001), it is common to observe discrepancies between both quantitative and semi-quantitative XRD concentrations and accurately-analyzed elemental chemistries (Hillier, 2000; Raven and Self, 2017). Given that clay

minerals and micas may comprise 50% by weight or more of black shale mineral content, to accurately quantify mineralogy of such rocks requires dealing with the preferred orientation problem.

One such approach, which has been applied to quantify shale mineralogy, is integration with elemental chemistry from other analytical techniques. The most common method for such determination in rocks and soils is X-ray fluorescence (XRF). As for XRD, XRF may be used for qualitative, semi-quantitative, or quantitative determinations, depending on factors including the instrument employed, whether and how calibration is performed, sample mounting, and analytical care in counting statistics and matrix correction. Quantitative XRF analysis is generally performed using wavelength-dispersive (WDS) rather than energy-dispersive (EDS) spectrometry (Zwicky and Lienemann, 2004). Required is a homogeneous sample of sufficient thickness to attenuate all primary x-rays from the instrument as well as samples of concentration known to high accuracy for calibration. XRF-determined concentrations of major elements are conventionally reported as oxides for major ions, including Na, K, Ca, Mg, Fe, Mn, Si, Al, Ti, and P, generally summed by convention to 100% of the total mass concentration of the sample.

In principle, these oxide concentrations might be used to at least estimate the underlying mineralogy. Indeed, in igneous petrology, elemental oxide concentrations have been used to estimate mineralogy by the so-called CIPW normative method that relies on a number of *a priori* assumptions and "rules of thumb", summarized in Kelsey (1965). However, in sedimentary petrology of shales, a heuristic basis is lacking for such normative procedures; there are simply too many possible combinations of silicates, clay minerals, and micas for a "rule of thumb" approach to be viable, due to provenance and other issues. In addition to the complexity of the mineral assemblages, there is the additional problem that such sediment often includes organic matter and, potentially, other amorphous phases (e.g. biogenic silica), resulting in fundamental

differences in mass basis between XRD and XRF. Nonetheless, the utility of integration between high-quality XRF and XRD datasets for quantification of mineral assemblages is apparent.

A number of previous investigations have used XRF either to aid in corroboration of XRD identifications or to support quantification of XRD results. Combinations of XRD and XRF microprobe mapping with other analytical tools (e.g. x-ray absorption near-edge spectroscopy, Fourier Transform Infrared spectroscopy, and Raman spectroscopy) have been used to differentiate carbonate species at low concentrations (Blanchard et al., 2016) and evaluate diagenesis (Piga et al., 2011). Synthesis of quantitative laboratory-based XRD and XRF results was used to evaluate the accuracy and precision of a portable XRD on known mixtures for application to the mineralogy of hydrothermal systems (Burkett et al., 2015). XRD-XRF data has also been used to assess weathering rates and subsequent soil formation (Ferrier et al., 2010), metallurgical ores (Hausen and Odekirk, 1991), and synthetic mixtures (Schorin and Carìas, 1987). It has also been suggested as a technique with multiple industrial applications (Loubser and Verryn, 2008). Despite these applications, little has been done to support quantifying mineralogy in fine-grained sedimentary rocks (Medrano and Piper, 1991).

The purpose of this investigation is to develop a normative-style procedure integrating XRD and high-accuracy WDS-XRF elemental oxide chemistries to produce quantitative mineral abundances for shales. Particular emphasis is placed on mineralogy of the Marcellus Shale (Devonian) of the Appalachian Basin. This will involve development of rule-based partitioning of XRF elemental masses according to XRD observations to estimate mineral concentrations, as well as some check on error between calculated and observed elemental mass balance. The correspondence between mineral abundance by a conventional semi-quantitative XRD-based method and this integrated XRF-XRD method will be examined.

2 Geologic Framework

Samples for this study were collected from a gas well in northeastern West Virginia from the Middle Devonian Marcellus Shale (Fig. 1). Within the study area, the Marcellus Shale is a ~30 m thick, heterogeneous formation dominated by gray to black, thinly-laminated, organic-rich shale. Bentonite layers, known as the Tioga Ashes, are found interbedded within the basal part of the Marcellus (Roen and Hosterman, 1982; Dennison and Textoris, 1988; Ver Straeten, 2004). The Marcellus is overlain by the Middle Devonian (Givetian) Mahantango Formation and underlain by the Onondaga Limestone (Fig. 2; Dennison and Hasson, 1976; Soeder et al., 2014). The Marcellus Shale and Mahantango Formation make up the Hamilton Group. Contacts above and below the Marcellus are gradational and marked by a change in gamma-ray response, indicating a transition from organic-rich to organic-poor facies (Soeder et al., 2014; Hupp, 2017).

The Marcellus was deposited from 394 to 389 Ma during the Acadian Orogeny within the Appalachian Basin of eastern North America (Parrish, 2013). At this time, oblique collision of Avalonia into the eastern margin of Laurentia formed the Acadian foreland basin in which fine-grained sediments of the Marcellus were deposited (Ettensohn, 1985; Ver Straeten, 2010; Hibbard et al., 2010; Lash and Engelder, 2011; Ettensohn and Lierman, 2013). Paleogeographic reconstructions indicate that the Acadian basin was located approximately 20-30° south of the paleoequator and was periodically inundated by the Kaskaskia Sea. The Marcellus Shale of West Virginia provides a record of distal sedimentation within this epeiric sea during a tectonically active period.

Marcellus lithologies are mudstone that reflect pelagic intrabasinal and clastic extrabasinal sedimentation under anoxic bottom-water conditions. Mineralogy in the Marcellus is diverse (Hupp, 2017), with total organic carbon (TOC) concentrations as high as 15% (Wang and Carr, 2013; Enomoto et al., 2014; Yu, 2015). In recent years, it has been the focus of

substantial economic interest due to its hydrocarbon production potential. Massive organic carbon burial associated with this unit has been cited as a key influence in the global cooling that occurred during the Eifelian into the Givetian (Ellwood et al., 2011). The high content of organic carbon and intrinsic diversity of mineralogy make the Marcellus Shale an ideal candidate for this study.

>>>Figures 1 and 2

3 Materials and Methods

3.1 Sampling and sample preparation

Fifty-five samples were collected by diamond-drill coring through the Marcellus (API # 47061017050000) in Monongalia County, West Virginia (Fig. 1). Horizontal side-wall mini-core samples were taken at intervals between 0.5 (15 cm) and 8.5 ft. (260 cm; average 1.7 ft., 52 cm) between depths 7455.0 ft. (2272.3 m) and 7556.2 ft. (2303.1 m) below land surface. Each 25-mm-diameter side-wall plug was 11 to 16 cm long of which the outer ends were used for geochemical characterization. The two end pieces were 1.5 to 6 cm long and together weighed from 10-50 g. Each sample was crushed into ~1 cm fragments, then pulverized for approximately 4 to 6 minutes using a Spex® Model 5100 steel shatterbox. This grinding duration was observed to produce powders with at least 65% of grains smaller than 100 μm. These powders were then split into two aliquots, one to be pressed using a hydraulic ram into Chemplex™ pellets for XRD and the other for XRF and organic/carbonate analysis.

3.2 X-ray Diffraction Analysis

Chemplex-mounted pressed-pellet sample disks were analyzed using a PANalytical X'Pert Pro™ X-ray Diffractometer with a CuK_{α} source at 2θ angles from 5° to 75° and a step time of

~12 seconds per degree (total scan time 13.5 minutes). X-rays were focused through a 20mm slit onto an Xcelerator™ detector. Samples were irradiated on a stage spinning at 1 revolution/second, with divergence and antiscatter slit angles of 0.5^{o} and 1°, respectively. The x-ray beam was operated at voltage 45 kV and current 40 mA. Mineral phases were qualitatively identified using the PDF2 reference library (ICDD, 2004) and PANalytical X'pert HighScore Plus©. Percentages were estimated semi-quantitatively using the reference-intensity ratio (RIR) matrix-flushing method (Chung, 1974a, 1974b) based on selected PDF2 reference samples chosen for each mineral phase (Table 1). For consistency, the same reference phases were employed for each mineral in all samples so that RIR concentrations were determined consistently between samples. No known amorphous phases were identified to be present in the sample except for organic matter. Therefore, the concentrations were on a weight-percent basis of the total inorganic (crystalline) fraction of the sample.

>>>Table 1

3.3 X-ray Fluorescence Analysis

XRF analysis was performed on the second aliquot of powders for all 121 samples to quantify both major, minor, and trace elements. 1.0 g of each powder was fused into 15 mm glass disks and analyzed for approximately three hours using a Thermo ARL Perform'X™ X-ray Fluorescence Spectrometer with a programmable aperture to measure a suite of 40 elements. Prior to fusion, all powders were analyzed by serial loss on ignition (LOI) at temperatures of 600°C and 900°C, to quantify organic matter and carbonates. The powders were heated overnight in glass crucibles within a programmable furnace.

To create the glass disks for analysis, 1 part powder and 2 parts fusion flux were combined in a vortex mixer and fused in a Merson grade UF-4S graphite crucible in an electronic furnace at 1000°C. Following first fusion, disks were cleaned, reground to a fine powder in a WC ring-

mill and fused again at 1000°C. Final glass disks are ultrasonically cleaned in ethanol prior to XRF analysis. Some elements are volatile during fusion and can lead to minima reports of Cl, S, Br, and As. Beads were then analyzed at an accelerating voltage of 45 kV at 45 mA. Crystalline material was kept at analyzation temperatures of 43°C and near constant pressure at 2.0 Pa. Accuracy, precision, and reproducibility were monitored by at least one repeat sample every ten samples as well as multiple certified reference standards simultaneously run including USGS AGV-2, BCR-2, BHVO-1, G-2, W-2, SDO-1, SCo-1, and STM-1.

Because the XRF analysis was completed on the LOI 900°C ashed samples, these concentrations are on a weight-percent basis of the total inorganic fraction. Some alteration of sample mineralogy was undoubtedly accomplished by the ashing, such as volatilization of water from clays and of CO_2 from carbonate minerals (calcite and dolomite). Other chemical elements would have essentially the same concentrations as the crystalline fraction of the XRD samples

3.4 Petrographic Analysis

Twenty-five thin sections were used to evaluate mineralogical phase expression within the Marcellus. Thin sections were prepared from selected 25 mm diameter sidewall plugs from the same set of samples as those taken for XRF and XRD analysis that had enough excess material. All thin sections were ground to the standard thickness of 30 microns. A Nikon ECLIPSE LV100N POL polarizing microscope was used for petrographic analysis.

4 Results

4.1 RIR XRD Mineralogy

Nine mineral phases were positively identified by XRD in the Marcellus samples: quartz, muscovite, illite, clinochlore (i.e., chlorite), pyrite, albite, calcite, dolomite, and barite (Table 1,

2). Powders analyzed by XRD were not treated to remove organic matter; however, organic matter does not refract X-rays according to Bragg's Law and thus XRD results only reflect crystalline mineral phases. These results are therefore expressed as a percentage of the crystalline fraction, only (Table 2).

Because the XRD patterns for illite and muscovite are indistinguishable from each other, the RIR-identified percentages for these phases are combined (e.g. "illite + muscovite") and their identification employed a single reference phase 01-082-0576. Petrographic evaluation of several Hamilton Group photomicrographs confirmed the presence of both phases (Fig. 3; Hupp, 2017). Illite was dominantly present within the mudstone matrices and appeared dark brown in color. Muscovite was distinguishable from the surrounding illite as euhedral, highly birefringent, elongate grains that were commonly ~50 μm in length.

>>>Figure 3

The RIR results are calculated to the nearest unit wt. % and sum to 100% ±1%. This analysis requires that each mineral's reference phase have a calculated RIR value. The error associated with RIR concentrations of unknown sample mixtures is not straightforward to estimate. Hillier (2000) found ranges of relative error (i.e., error divided by concentration) from a few percent to as high as 100% using RIR, with the higher errors associated with minerals at lower, near-detection limit concentrations.

>>>Table 2

4.2 XRF Elemental Chemistry

Results of quantitative XRF analysis are shown in Table 3 for elemental oxides (SiO_2, Al_2O_3, FeO, MgO, CaO, Na_2O, K_2O, BaO, SrO, and SO_3) in wt. % of the fraction including these elements plus LOI 600°C, the mass of volatilized organic matter, and LOI 900°C, the mass

volatilized from decarbonation of carbonate minerals. This mass basis was selected to mirror that employed for the XRD estimates as closely as possible. Barium (on average >1.05 %) and strontium were included in this set as they were both in high concentration in a trace-element suite run on the same samples. The strong correlation (R^2=0.979; Fig. 4) observed between the more elevated XRF BaO and SrO concentrations suggest they may well be present in the same mineral phase. Ba reaches high concentrations (>15% as BaO) in one sample, and in fact barite was identified in some, but not all, XRD samples, specifically those with higher concentrations. In the other samples, barite is either below detection, or not present while Ba occurs in other phases, presumably carbonates. SrO is generally one or more orders of magnitude lower than BaO in molar concentration, and, because strontianite mineral phases are absent or non-detectable, there is a good possibility that where barite is identified, it is strontian, similar to observations by other investigators (He et al., 2014). The average mass ratio of BaO: SrO is about 19:1, although Fig. 4 suggests that at higher barite concentrations the ratio is closer to 106:1. Thus barite is interpreted to contain an estimated 1-5% Sr substitution for Ba at different concentration levels.

The powders used for XRF were first ashed to 900° C for loss on ignition (LOI) analysis; the wt. % of LOI 600°C (approximately equal to organic matter) and 900°C (approximately equal to CO_2 lost from carbonate minerals) are also included in Table 3. Thus the XRF samples had all organic matter and carbonate CO_2 removed prior to analysis. Because no amorphous phases were observed in the samples, it is believed that only the crystalline fraction of the bulk rock was analyzed for elemental chemistry with calcite and dolomite decarbonated to oxides. Only elements interpreted to be present in mineral(s) identified by XRD are included in the data of Table 3. Additional elements were analyzed, including TiO_2 (<0.8%), MnO (<0.06%), P_2O_5

(<0.2%), and a number of trace elements (sum=<0.42%); however, the average concentration for these additional constituents was <1.0% per sample, and so they were simply excluded from the analysis and are not reported. The results of Table 3 are normalized to 100% of the reported oxides, plus the lost CO_2 from carbonate minerals represented by LOI 900° C. On this basis, the elemental concentrations correspond very closely to the 100% basis for the crystalline fraction in XRD analysis.

>>>Table 3 and Figure 4

4.3 XRD-XRF data integration

Quantitative mineralogy was estimated employing the inherently more accurate XRF elemental concentrations, allowing comparison to the semi-quantitative RIR estimates (Tables 2, 4). The abundance of each mineral phase identified was recalculated based on the XRF results, by employing the stoichiometries of each corresponding PDF2 reference phase identified in each sample by XRD (Table 1). For some mineral phases, elements in the XRF suite occur only in that phase; for example, among the phases identified, only albite contains Na, neglecting trace substitution of Na into cationic structural positions within other phases. Besides Na, other elements in this class include Ba + Sr (barite), and K (muscovite + illite). For all other minerals, elements present in abundance contribute to more than one phase, including Ca (calcite, dolomite), Mg (dolomite, chlorite), Fe (pyrite, chlorite), Al (all aluminosilicate phases), and Si (quartz and all aluminosilicate phases). To partition XRF concentrations across the mineral suite, a sequential procedure was needed, subject to the fact that both XRD and XRF concentrations sum to 100% of the crystalline (excluding organic) fraction. This serial approach first implements the single-phase elements, then the multiple-phase elements. Steps in this approach include:

1. All K is present either in muscovite or illite, not easily discriminated by XRD, so "muscovite + illite" is quantified together using total K
2. All Na is present in albite, so total Na determines albite %
3. SrO + BaO concentrations are used to determine barite %.
4. MgO is partitioned between chlorite % and dolomite %, proportional to the ratios of the (001) and (104) peak heights, respectively. If no chlorite is observed by XRD then all Mg is used for dolomite, and vice versa.
5. All residual FeO, after subtracting FeO from the Mg-determined chlorite %, is used to determine pyrite %.
6. All residual CaO, after subtracting that within dolomite %, is used to determine calcite %. If the resulting calcite Ca is negative, it is set as zero
7. SiO_2 is partitioned between quartz, albite, chlorite, and muscovite + illite according to steps 1, 2 and 4 above, with quartz % determined from the residual after subtracting the sum of alumniosilicate SiO_2.
8. The sum of crystalline components, excluding organic matter, is normalized to 100%.

There are implicit assumptions in this procedure, the most significant of which are (a) the lack of isomorphous solid state substitution for cations, and (b) neglection of adsorbed cations on clays. The procedure is primarily an exercise in mass balance and mineral stoichiometry. In detail, for single phase elements (e.g. Na, K, and Ba + Sr), mineral concentrations for albite, muscovite + illite, and barite, respectively, were calculated as follows:

$$X_{min} = X_{ox} [G_{min}/(n*G_{ox})] \quad (1)$$

where:

X_{min} = weight percent of mineral phase

X_{ox} = weight percent of the XRF-determined elemental oxide

G_{min} = gram formula weight of the mineral phase

G_{ox} = gram formula weight of the elemental oxide

n = ratio of moles of element in mineral phase to moles in the oxide

For example, XRF K_2O (2 moles K) applied to XRD muscovite/illite (reference stoichiometry $KAl_2(AlSi_3)O_{10}(OH)_2$) yields n= 0.5. These equations are applied in steps 1-3 above to determine muscovite + illite, albite, and strontian barite concentrations.

In step 4, for samples with detectable concentrations of both chlorite and dolomite, MgO is partitioned between these two phases (1=chlorite, 2 = dolomite) according to R_{12}, the ratio of baseline-corrected peak-height counts per second (cps) for chlorite to dolomite:

$$X_{chl} = X_{MgO}*[R_{12}/(R_{12}+1)]*[G_{chl}/(2.5G_{MgO})] \quad (2)$$

$$X_{dol} = X_{MgO}*[1/(R_{12}+1)]*[G_{dol}/G_{MgO}] \quad (3)$$

In addition to having a partition with Mg, chlorite and dolomite also partition Fe and Ca with pyrite and calcite, respectively. For these two elements, the concentrations as an elemental oxide partitioned into minerals in equations (2) and (3) may be subtracted from the total XRF FeO and CaO, respectively:

$$X_{pyr} =[X_{FeO} - X_{chl} *(G_{FeO}/G_{chl})]*(G_{chl}/G_{FeO}) \quad (4)$$

$$X_{cal} =[X_{CaO} - X_{dol} *(G_{CaO}/G_{dol})]*(G_{cal}/G_{CaO}) \quad (5)$$

where the X notation describes mineral concentrations or wt. % oxide and the G values are formula weights of either minerals or XRF oxides.

Once steps 1 to 6 were complete, in step 7 residual SiO_2 was used to estimate silica in quartz after all SiO_2 partitioned into silicate phases was summed, according to stoichiometries.

$$X_{qtz} = X_{SiO2} - G_{SiO2} [2.2X_{chl} /G_{chl} + 3X_{mus}/G_{mus} + 3X_{alb} /G_{alb}] \quad (6)$$

307 Then the absolute abundance of each mineral phase (X_m) as a portion of the inorganic fraction is
308 calculated by normalizing the mineral abundances to 100%.
309 Similarly, using the normalized XRD-XRF quantification, Al_2O_3 may be calculated from the
310 silicate mineral concentrations:

311 $$X_{Al2O3} = G_{Al2O3} [1.65X_{chl}/G_{chl} + 1.5X_{mus}/G_{mus} +0.5X_{alb}/G_{alb}] \quad (7)$$

312 The results of this procedure are presented in Table 4 and are based on both the XRD
313 results (identity of minerals found, peak-height ratio of chlorite to dolomite if both are present)
314 and XRF elemental concentrations. These results will be referred to as XRD-XRF mineralogy.
315 Implementing the partitioning procedure encountered minor difficulties on the Marcellus
316 samples. In two samples (7505.0 and 7538.0), calcite concentration calculated by XRD-XRF
317 was slightly negative but within 1% of zero. These were both samples in which only minor
318 concentrations calcite had been detected by XRD. These XRD-XRF calcite values were set to
319 zero. In all samples with no XRD detectable peaks for chlorite or dolomite , both were set to
320 zero and the XRF MgO was not employed, despite minor (<1.0%) MgO being present by XRF.
321 Similarly, zero values for XRD-XRF concentration of both dolomite and calcite were honored in
322 three such cases (7485.6, 7523.0, 7554.4) and XRF CaO was not employed. Any resulting mass
323 balance error was removed by normalization. The cause for these anomalous results is ascribed
324 to (1) the potential for minor concentrations of Mg, Na, and Ca as adsorbed cations on clays or as
325 trace substitutions for other cations in minerals or (2) difficulty in detecting and quantifying
326 calcite or, especially, dolomite by XRD at low levels.
327 Figure 5 shows a plot of XRD traces of four type lithologies occurring within the core.
328 From top to bottom, these are a calcareous mudstone; a non-calcareous mudstone; a highly-
329 calcareous mudstone; and a muddy limestone. Most peaks used for identification lie in the 7-50

degree 2 theta region. The top 2 lithologies are relatively common in the core, while the bottom 2 show more unusual high-barite and high-calcite suites. Minerals that are generally abundant where present include quartz, illite/muscovite, and chlorite. Calcite and dolomite may be present or absent and, except in unusual limey samples such as 7554.3 ft., in low concentration. Pyrite and albite are present throughout, but in minor concentrations. Barite is generally absent but, where found, is often rather abundant and shows multiple peaks on the diffractogram, as in 7544.4 ft.. These samples emphasize the greater ease in detecting more abundant phases (quartz, clays) than those with minor peaks, especially albite, pyrite, and dolomite.

Figure 6 shows a boxplot of XRD-XRF mineralogy results for all samples, showing median (thick horizontal band), the middle 2 quartiles of frequency (box) and minima/maxima ("whiskers"). Quartz and muscovite+illite are the dominant minerals in most samples, although their low minima suggest a few low values. The rest of the minerals are less abundant, although calcite and dolomite appear to have a few very high outliers and are likely non-normally distributed. Chlorite, pyrite, albite, and dolomite all have medians in the 1-10 wt. % range and no extreme outliers. Thus, the mineralogy has three dominant phases and the rest minor, although calcite and barite appear to be very high in some samples.

>>>Table 4; Figures 5 and 6

4.4 Comparison of XRD-XRF to RIR results

Figure 7 compares XRD-XRF to RIR results for quartz (top) and summed clay minerals muscovite/illite plus chlorite (bottom). Together, these minerals constitute an average of 72.9% and 78.0% of the crystalline fraction in the XRD-XRF and RIR datasets, respectively. That is, these minerals represent the majority of crystalline matter present, with other phases, except in outlier samples, at relatively minor concentrations. The dashed line is unit slope and the solid

line a linear regression fit. Both mineral sets show modest correlation but with a large amount of scatter. Significantly, in virtually all of the samples, quartz lies above the dashed line, indicating that XRD-XRF estimates quartz content higher than RIR, and the converse for the clay minerals. RIR has a significant high bias with respect to phyllosilicates compared to XRD-XRF and a significantly low bias with respect to quartz. Given these are the two major components of mineral abundance in this suite, it is clear that underestimation of one enhances and/or causes overestimation of the other, or vice versa, due to the concentrations being closed to 100% in both cases. It may be concluded that (1) the correlations between both quartz and clay minerals for the two methods of interpretation are present, but not highly significant and (2) RIR interpretation has a positive bias for clay minerals and a negative for quartz, with respect to the XRD-XRF method. From these results, it is not clear which of the two methods is more accurate, and it is likely that both have error.

>>>Figure 7

Figure 8 shows XRF Al_2O_3 vs XRD-XRF Al_2O_3, with the latter calculated from the concentration in the lower plot of Figure 7 plus albite, the only other silicate phase. The correlation (R^2=0.989) is high and linear. One might examine a similar plot for SiO2 using these minerals plus quartz, but this trivial case would be completely linear because, by the XRD-XRF procedure, all XRF SiO_2 is partitioned among these phases, *de facto*. Thus Figure 8 demonstrates that the XRD-XRF mineralogy is in excellent agreement with XRF values of Al_2O_3 as well as SiO_2.

>>>Figure 8

Figure 9 compares XRD-XRF to RIR mineral concentrations for quartz, muscovite, calcite, and pyrite. Only weak correlations are present for all except calcite, which is highly

correlated (R^2=0.969) between the two methods. Similar to Figure 7, quartz is underestimated and muscovite overestimated by RIR. Pyrite tends to be underestimated at low concentration and overestimated at high concentration.

>>>Figure 9

Figure 10 shows similar plots for minor phases such as chlorite, albite, dolomite, and barite. Barite, the highest in concentration, shows the best correlation and is underestimated by RIR, though in a linear fashion. The other minerals show grouping of RIR concentrations at integer values due to its low precision. Albite and dolomite show very low correlation and most values below 3% by RIR. Chlorite seems to show moderate correlation at higher concentrations, perhaps related to the fact that its 7.08 Å (001) peak is unambiguous and not obfuscated by other minerals' lines.

>>>Figure 10

Comparison of RIR to XRD-XRF suggests some clear observations. First, there are only general correlations for most phases, excepting calcite and barite, and the two interpretations are not perfect predictors of each other. Second, the RIR results consistently overestimate clay mineral abundances and overestimate quartz abundances compared to XRD-XRF. Third, the XRD-XRF calculated Al_2O_3 are in excellent agreement with the XRF data values, despite the latter not having been directly employed in the procedure. This provides one of the few checks available on the analysis for unknown samples.

4.5 Classification of XRD mineralogical facies

To explore groupings within the dataset, cluster analysis was performed on all 55 samples using Wards agglomerative D2 hierarchical clustering method (Murtagh and Legendre, 2014). The dendrogram for this analysis (Fig. 11) is labeled according to sample depth. A cut of the

dendrogram at k=4 clusters was performed, yielding two large clusters (n=24, 23; clusters 1 and 2) at the bottom of Figure 12 and two relatively small clusters (n=6, 2; clusters 3 and 4) at the top. Circular plots of mineral concentrations for centroids of these clusters are shown in Figure 12 with average mineral concentrations for each cluster outlined in Table 5. The large and small clusters are discussed separately.

>>>Table 5; Figures 11 and 12

Clusters 1 and 2 are quite similar to each other in that quartz and muscovite constitute 70-75% of the centroid abundance. Of the other phases, pyrite, albite and barite are also similar between the two facies, with barite occurring in trace concentration and pyrite and albite about 10% and 6%, respectively. Petrographic analysis of samples from these clusters do not show obvious differences (Fig. 13).

The only consistent differences within the two facies are in the minerals chlorite, dolomite, and calcite. In cluster 1, chlorite is nearly absent, while calcite and dolomite are present in similar concentrations. In cluster 2, calcite and dolomite are nearly absent and chlorite accounts for about 9%. The cluster 1 samples are concentrated in the lower Marcellus (7503.0-7556.0) while the cluster 2 samples are at the top (7455.0-7500.0). There is little overlap. The upper Marcellus samples are therefore chloritic mudstones, while the lower Marcellus contains calcareous mudstones. When chlorite is present, dolomite is largely absent, and vice versa.

Clusters 3 and 4 are both small groups that seem anomalous. Cluster 3 is a quartz-muscovite mudstone with higher concentrations of the other mineral phases, in particular calcite and/or barite. Cluster 4 comprises only 2 samples and is 75% calcite with minor quartz and barite. Thus cluster 3 is a highly-calcareous mudstone and cluster 4 a muddy limestone. Petrographic analysis of these clusters show that samples within cluster 4 exhibit an abundance of fossils,

primarily styliolinids and thin-walled mollusc shells, within a matrix composed of clay and displacive calcite (Fig. 13). Fossils display both drusy and blocky cements within the larger intragranular pores. A dolomite vein also runs through one of the two samples. These two observations help to account for the abundant carbonate content. Photomicrographs of cluster 3 samples are dominated by an illite-muscovite matrix with sparse fossil-rich lamina or carbonate-replaced radiolaria. Differences in matrix composition, biogenic sediments, and diagenetic phases likely account for the separate clustering among these samples.

>>>Figure 13

Figure 14 shows barplots of mineral distributions in various clusters. Quartz and muscovite are highest in clusters 1 and 2, lower in cluster 3, and very low in the limestone cluster. Calcite and barite are both present in the anomalous clusters 3 and 4. Pyrite and albite tend to be similar in concentration in clusters 1-3 and lowest in the limestone. Chlorite and dolomite show inverse abundance in cluster 1 and 2 mudstones and are absent in cluster 4.

>>>Figure 14

5 Discussion

5.1 Comparisons of RIR- and XRD-XRF-derived mineralogy

Comparison of the RIR to XRD-XRF mineralogy results clearly indicate that for all phases except calcite and barite, the two quantitative sets are in only general agreement, with significant differences between the two. Correlations are poorest for the minerals dolomite and albite, both of which occur at RIR concentrations below 6% and in many cases ≤3%, which is arguably the lower detection limit of RIR methodology.

It is clear, as well, that the RIR method overestimates clay minerals and underestimates quartz in comparison to XRD-XRF. We interpret this to likely be the result of exaggeration of

XRD peak heights for clay minerals and mica due to preferred sample orientation. This is supported by the observation that SiO_2 from XRF and from XRD-XRF mineralogy are (de facto) consistent, but in addition Al_2O_3 is highly consistent between the two datasets, by mass balance, despite the fact that alumina from the XRF dataset were not employed in the XRD-XRF procedure. These observations support the interpretation that the XRD-XRF values are inherently more accurate than the RIR interpretations. They are also less arbitrary, as the uncalibrated RIR results are based on a somewhat arbitrary selection of reference samples and RIR parameters.

5.2 Applications and limitations of cross-quantification methodology

There are some issues with the XRD-XRF results in this dataset for minerals present at low concentration, especially albite, dolomite, and calcite. Besides simple higher relative error at low concentration, these issues are possibly related to concentrations of adsorbed cations on clays not being measured and considered, and while this adsorbed cation fraction is unlikely to have been large, neglecting it could have an effect on low-concentration minerals in the calculation method. The simplest solution to this problem would be to displace adsorbed cations with a cation not measured by XRF, such as ammonium, prior to XRF analysis. This could ensure that the elemental analysis is performed on a fraction containing only crystalline inorganic compounds.

The XRD-XRF method in this investigation was based upon a set of rules that appears to have been successful for this particular mineral suite, presenting a potential quantitative approach for establishing mineralogy in marine shales. The XRD-XRF workflow incorporates data sets that are often required for further interpretation of mudstones and presents a methodology for determining bulk mineralogy within rocks of multiple unknown phases.

However, the presence of multiple minerals containing a single element is a complication that needs to be worked out for dataset-specific conditions, on a case by case basis.

5.3 Marcellus mineralogy

Quartz, illite+muscovite, and albite covary and are inversely correlated with calcite and dolomite; that is, there are distinct siliciclastic and calcareous mudstone zones that occur in the top and bottom, respectively, of the Marcellus (Table 4). Key indicator minerals of this difference in mineralogy are chlorite, dolomite, and calcite. Of minerals containing Mg, chlorite dominates the upper siliclastic zone, whereas dolomite dominates the calcareous zone, with a thin interval in the middle (7488.0-7500.6 ft.; 2282.3-2286.2 m) in which both minerals occur (Fig. 15). The transition from dolomite to chlorite could reflect changes in sediment provenance and perhaps influx from a metasedimentary source. Chlorite could also have been produced by hydrothermal alteration of muscovite, influenced by Mg-rich brines that have been reported within the Marcellus (Haluszczak et al., 2013). However, it seems unlikely that such brine alteration or metamorphism would only produce chlorite in the upper part of the Marcellus and not affect muscovite within the lower section. The consistent occurrence of chlorite within the upper Marcellus suggests that chlorite may be a primary extrabasinal mineral phase.

The transition from cluster 1 mineralogy in the lower Marcellus to cluster 2 in the chloritic upper zone possibly reflects changes in sedimentation patterns from pelagic-dominated to hemipelagic-dominated sedimentation. Clusters 1, 3, and 4 in the calcareous lower Marcellus may, correspondingly, reflect an intrabasinal provenance. Comparison of stratigraphic cluster distribution to total organic carbon (TOC) content indicates lower TOC values are correlative to the onset of cluster 2 mineralogical deposition (Fig. 15). These observations suggest that the

mineralogy of the Marcellus may be indicating primary depositional influences on organic carbon preservation.

>>>Figure 15

5.4 Errors and uncertainty in XRD-XRF results

While the XRD-XRF approach resolves some well-known difficulties in XRD interpretation, there are still potentials for error in implementation:

1. The method depends on accurate and complete identification of all crystalline phases present, as does the RIR and other methods.
2. XRF analysis may include concentrations of elements that are not within the crystalline fraction, but in amorphous phases, organic matter, or adsorption sites on clays. Care must be taken to identify, pre-treat, or correct for such concentrations, so that the basis for both XRD and XRF analyses are close to identical. This is especially the case for elements in low abundance, as Ca, Mg, and Na were in some of the Marcellus samples.
3. The stoichiometry of the identified minerals must match that of the phase in the sample itself. In this investigation, the idealized reference PDF formulae were employed. This is subject to error, particularly with respect to deviations from ideal caused by trace substitution. A better approach may be to individually characterize crystal chemistries using SEM or microprobe methods.

In XRD interpretation, the relative error tends to be greatest for phases in minor concentration. This is likely to remain true for application of XRD-XRF integration.

6 Conclusions

Traditional XRD methodologies commonly produce semi-quantitative results and are subject to error in quantifying minerals that show preferred orientations (e.g. clay minerals and mica). Here we produce a workflow for quantitatively determining mineralogy via integration of XRD and XRF data sets using marine mudstones from the Marcellus Shale. Key findings include:

- Nine mineral phases were identified in some or all samples including quartz, muscovite, illite, pyrite, chlorite, albite, calcite, dolomite, and barite.
- XRD-XRF integration allowed determination of quantitative mineral abundances for all 55 samples, correcting for overestimation of clays and mica (i.e. illite+muscovite) produced using XRD results alone.
- Cluster analysis of XRD-XRF mineralogy identified 4 mineralogical facies within the Marcellus that may reflect potential depositional influences on differences in organic matter content between the upper and lower Marcellus.

The technique may be broadly applicable to the determination of mineralogy in shale and mudstone, although it is likely to require modification of the sequential approach to handle different mineral assemblages. This methodology would also benefit from analytical characterization of mineral stoichiometry, rather than using ideal formulae.

Acknowledgements

This research was funded by the USDOE National Energy Technology Laboratory as part of the Marcellus Shale Energy and Environmental Laboratory project (MSEEL; Award DE-FE0024297). We acknowledge Northeast Natural Energy LLC for providing access to the core material. Contractual elemental chemistry was performed using x-ray fluorescence and loss-on-

ignition by Rick Conrey and Laureen Wagoner of the Hamilton Analytical Laboratory, Taylor Science Center, Hamilton College.

References

Blanchard, P.E.R., Grosvenor, A.P., Rowson, J., Hughes, K., Brown, C., 2016. Identifying calcium-containing mineral species in the HEB Tailings Management Facility at McClean Lake, Saskatchewan. Applied Geochemistry 73, 98-108.

Braun, G.E., 1986. Quantitative analysis of mineral mixtures using linear programming. Clays and Clay Minerals 34, 330-337.

Burkett, D.A., Graham, I.T., and Ward, C.R., 2015. The application of portable x-ray diffraction to quantitative mineralogical analysis of hydrothermal systems. Canadian Mineralogist 53, 429-454.

Chung, F.H., 1975a. Quantitative interpretation of x-ray diffraction patterns of mixtures. III. Simultaneous determination of a set of reference intensities. Journal of Applied Crystallography 8, 17-19.

Chung, F.H., 1975b. Quantitative interpretation of x-ray diffraction patterns of mixtures. I. Matrix-flushing method for quantitative multicomponent analysis. Journal of Applied Crystallography 7, 519-525.

da Silva, A. L., de Oliveira, A.H., and Fernandes, M.L.S., 2011. Influence of preferred orientation of mineral in the mineralogical identification process by x-ray diffraction. International Nuclear Atlantic Conference-INAC 2011 Proceedings. Associacao Brasileira de Energia Nuclear, 11 p.

Dennison, J.M. and Hasson, K.O., 1976. Stratigraphic cross-section of Hamilton Group (Devonian) and adjacent strata along south border of Pennsylvania. The American Association of Petroleum Geologists Bulletin 60, 278-298.

Dennison, J.M., and Textoris, D.A., 1988. Devonian Tioga ash beds. West Virginia Geological and Economic Survey Circular, 15-16.

Ellwood, B.B., Algeo, T.J., Hassani, A.E., Tomkin, J.H., and Rowe, H.D., 2011. Defining the timing and duration of the Kacak Interval within the Eifelian/Givetian boundary GSSP, Mech Irdance, Morocco, using geochemical and magnetic susceptibility patterns. Palaeogeography, Palaeoclimatology, Palaeoecology 304, 74-84.

Enomoto, C.B., Olea, R.A., and Coleman, J.L. Jr., 2014. Characterization of the Marcellus Shale based on computer-assisted correlations of wireline logs in Virginia and West Virginia. US Geological Survey-Scientific Investigations Report, 21 p.

Ettensohn, F.R., 1985. The Catskill Delta complex and the Acadian Orogeny; a model. Geological Society of America Special Paper No. 201, 39-50.

Ettensohn, F.R., and Lierman, T.R., 2013. Large scale tectonic controls on the origin of Paleozoic dark shale source rock basins; examples from the Appalachian foreland basin, Eastern United States. American Association of Petroleum Geologists Memoir 100, 95-124.

Ferrier, K.L., Kirchner, J.W., Riebe, C.S., and Finkel, R.C., 2010. Mineral-specific chemical weathering rates over millennial timescales: Measurements at Rio Icacos, Puerto Rico. Chemical Geology 277, 101-114.

Grattin-Bellew, P.E., 1975. Effects of Preferred Orientation on X-ray Diffraction Patterns of Gypsum. American Mineralogist 60, 1127-1129.

Haluszczak, L.O., Rose, A.W., and Kump, L.R., 2013. Geochemical evaluation of flowback brine from Marcellus gas wells in Pennsylvania, USA. Applied Geochemistry 28, 55-61.

Hausen, D.M., and Odekirk, J.R., 1991. XRD mineralogic logging of drill samples from gold and copper mining operations. Ore Geology Reviews 6, 107-118.

He, C., Li, M., Liu, W., Barbot, E., Vidic, R.D., 2014. Kinetics and equilibrium of barium and strontium sulfate formation in Marcellus Shale flowback water. Journal of Environmental Engineering paper B4014001, 1-9.

Hibbard, J.P., van Staal, C.R., and Rankin, D.W., 2010. Comparative analysis of the geological evolution of the northern and southern Appalachian orogeny Late Ordovician-Permian. Geological Society of America Memoir 206, 51-69.

Hillier, S., 2000. Accurate quantitative analysis of clay and other minerals in sandstones by XRD: comparison of a Rietveld and a reference intensity ratio (RIR) method and the importance of sample preparation. Clay Minerals 35, 291-302.

Hupp, B.N., 2017. Provenance of the Hamilton Group: A study of source-to-sink relationships within the Middle Devonian central Appalachian Basin. M.S. Thesis, West Virginia University, Morgantown, West Virginia, USA, 128 p.

International Center for Diffraction Data (ICDD), 2004, PDF-2 diffraction database.

Jenkins, R., 1989. Experimental procedures. In: D.J. Bish and J.E. Post (Eds.), Modern Powder Diffraction: Reviews in Mineralogy 20. Mineralogical Society of America, Washington, D.C., pp. 47–71.

Kelsey, C.H., 1965. Calculation of the C.I.P.W. norm. Mineralogical Magazine 34, 276-282.

Klug, H.P., and Alexander, L.E.,1974. X-ray diffraction procedures: For polycrystalline and amorphous materials, 2nd edition. New York, John Wiley & Sons, 992 p.

Kolka, R.K., Laird, D.A., Nater, E.A., 1994. Comparison of four elemental mass balance methods for clay mineral quantification. Clays and Clay Minerals 42, 437-443.

Lash, G.G., and Engelder, T., 2011. Thickness trends and sequence stratigraphy of the Middle Devonian Marcellus Formation, Appalachian Basin: Implications for Acadian foreland basin evolution. American Association of Petroleum Geologists Bulletin 95, 61-103.

Loubser, M., and Verryn, S., 2008. Combining XRF and XRD analyses and sample preparation to solve mineralogical problems. South African Journal of Geology 111, 229-238.

Medrano, M.D., and Piper, D.Z., 1991. A normative-calculation procedure used to determine mineral abundances in rocks from the Montpelier Canyon Section of the Phosphoria Formation, Idaho: A tool in deciphering the minor-element geochemistry of sedimentary rocks. US Geological Survey Bulletin 2023A.

Milici, R.C., and Swezey, C.S., 2014. Assessment of Appalachian basin oil and gas resources; Devonian gas shales of the Devonian Shale-Middle and Upper Paleozoic total petroleum system. U.S. Geological Survey Professional Paper 1708.

Murtagh, F., and Legendre, P., 2014. Ward's hierarchical agglomerative clustering method: which algorithms implement Ward's criterion?. Journal of Classification 31, 274–295.

Paronish, T., 2018, Meso- and macro-scale facies and chemostratigraphic analysis of Middle Devonian Marcellus Shale in northern West Virginia, USA. M.S. Thesis, West Virginia University, Morgantown, West Virginia, USA.

Parrish, C.B., 2013. Insights into the Appalachian Basin Middle Devonian depositional system from U-Pb Zircon geochronology of volcanic ashes in the Marcellus Shale and Onondaga Limestone. M.S. Thesis, West Virginia University, Morgantown, West Virginia, USA, 149 p.

Piga, G., Santos-Cubedo, A., Brunetti, A., Piccinini, M., Malgosa, A., Napolitano, E., and Enzo, S., 2011. A multi-technique approach by XRD, XRF, FT-IR to characterize the

diagenesis of dinosaur bones from Spain. Palaeogeography, Palaeoclimatology, Palaeoecology 310, 92-107.

Poppe, L.J., Paskerevich, V.F., Hathaway, J.C., and Blackwood, D.S., 2001. A laboratory manual for x-ray powder diffraction. US Geological Survey Open-File Report 01-041.

Potter, P.E., Maynard, J.B., and Depetris, P.J., 2005. Mud and Mudstones, Introduction and Overview, Berlin, Springer, 297 p.

Raven, M.D. and Self, P.G., 2017. Outcomes of 12 years of the Reynolds Cup quantitative mineral analysis round robin. Clays and Clay Minerals 65, 122-134.

Roen, J.B., and Hosterman, J.W., 1982. Misuse of the term “bentonite” for ash beds of Devonian age in the Appalachian basin. Geological Society of America Bulletin 93, 921-925.

Saupe, F., and Vegas, G., 1987. Chemical and mineralogical compositions of black shales (Middle Palaeozoic of the Central Pyrenees, Haute-Garonne, France). Mineralogical Magazine 51, 357-369.

Schorin, H. and Carías, O., 1987. Analysis of natural and beneficiated ferruginous bauxites by both x-ray diffraction and x-ray fluorescence. Chemical Geology 60, 199-204.

Soeder, D.J., Enomoto, C.B., and Cermak, J.A., 2014. The Devonian Marcellus Shale and Millboro Shale. The Geological Society of America Field Guide 35, 129-160.

Srodon, J., Drits, V.A., McCarty, D.K., Hsieh, J.C.C., and Eberl, D.D., 2001. Quantitative x-ray diffraction analysis of clay-bearing rocks from random preparations. Clay and Clay Minerals 49, 514-528.

Ver Straeten, C.A., 2004. K-bentonites, volcanic ash preservation, and implications for Early to Middle Devonian volcanism in the Acadian orogen, eastern North America. Geological Society of America Bulletin 116, 474-489.

Ver Straeten, C.A., 2010. Lessons from the foreland basin: Northern Appalachian basin perspectives on the Acadian orogeny. The Geological Society of America Memoir 206, 251-282.

Wang, G., and Carr, T.R., 2013. Organic-rich Marcellus Shale lithofacies modeling and distribution pattern analysis in the Appalachian Basin. American Association of Petroleum Geologists Bulletin 97, 2173-2205.

Yu, W., 2015. Developments in modeling and optimization of production in unconventional oil and has reservoirs. Ph.D. Dissertation, University of Texas at Austin, Austin, Texas, USA, 264 p.

Zhou, C.H., and Keeling, J., 2013. Fundamental and applied research on clay minerals: from climate and environment to nanotechnology. Applied Clay Science 74, 3-9.

Zwicky, C.N., and Lienemann, P., 2004. Quantitative or semi-quantitative? Laboratory-based WD-XRF versus portable ED-XRF spectrometer: results obtained from measurements on nickel-base alloys. X-ray Spectrometry 33, 294-300.

Table Titles

1. Mineralogical information from the PDF2 reference library (ICDD, 2004)
2. RIR XRD mineralogy results reported as % of the bulk rock crystalline fraction.
3. XRF results reported as wt. % of each oxide and wt. % mass loss during each burn at 600°C and 900°C.
4. Quantitative mineralogy determined via XRD-XRF integration reported as % of the crystalline fraction.
5. Mean and standard deviation of mineral phases for each cluster.

Figure Captions

1. Map showing the location of the study area with the state of West Virginia marked in dark gray (large map). Location of the sampled well (star) and the approximate thickness of the Marcellus Shale in the central Appalachian Basin region shown in the small inset. (50-99 ft.=15.2-30.2 m; 100 ft.=30.5 m) Thickness data from Milici and Swezey, 2014.
2. Stratigraphic column showing regional Appalachian stratigraphy with accompanying gamma-ray log from the sampled well.
3. Photomicrograph in plane polarized light showing euhedral muscovite (large arrows) and detrital quartz grains (small arrows) within an illite-rich matrix.
4. Plot of XRF-determined BaO vs CaO in Marcellus samples, as weight percent of the 900°C ashed samples.
5. X-ray diffraction traces of typical sample of (a) non-calcareous mudstone, (b) calcareous mudstone, (c) carbonate-rich mudstone, and (d) silty limestone. Legend:

M=muscovite+illite; Chl=chlorite; Q=quartz; B=barite; P=pyrite; C=calcite; D=dolomite; A=albite. Sample IDs indicated at upper right of plots.

6. Boxplot of XRD-XRF mineralogy for all samples, as percent of crystalline fraction. Median is the black horizontal bar; box is the central 50% of sample frequency. Whisker ends are minima and maxima.
7. Comparison of quartz (top) and clay mineral sum (bottom) between RIR and XRD-XRF interpretations, in percent of crystalline fraction.
8. Comparison of Al_2O_3 from XRF and calculated Al_2O_3 from XRD/XRD mineralogy. sum (bottom) between RIR and XRD-XRF interpretations, in percent of crystalline fraction.
9. Comparison of (in clockwise direction) quartz, muscovite+illite, calcite, and pyrite between RIR and XRD-XRF interpretations, in percent of crystalline fraction.
10. Comparison of in clockwise direction) chlorite, albite, dolomite, and barite between RIR and XRD-XRF interpretations, in percent of crystalline fraction.
11. Dendrogram for cluster analysis, showing 4-cluster groupings. Sample labels are depth in feet.
12. Circle charts of mineral concentration for cluster centroids, in percent of crystalline fraction.
13. Photomicrograph examples from each mineralogical cluster with A-D synonymous to clusters 1-4.
14. Boxplots of mineral concentration for cluster centroids, in percent of crystalline fraction.
15. Mineralogical cluster, quartz, illite+muscovite, chlorite, and dolomite stratigraphic distribution paired with uranium-predicted total organic carbon (TOC) log from the sampled well (Paronish, 2018).

Figure 1
Click here to download high resolution image

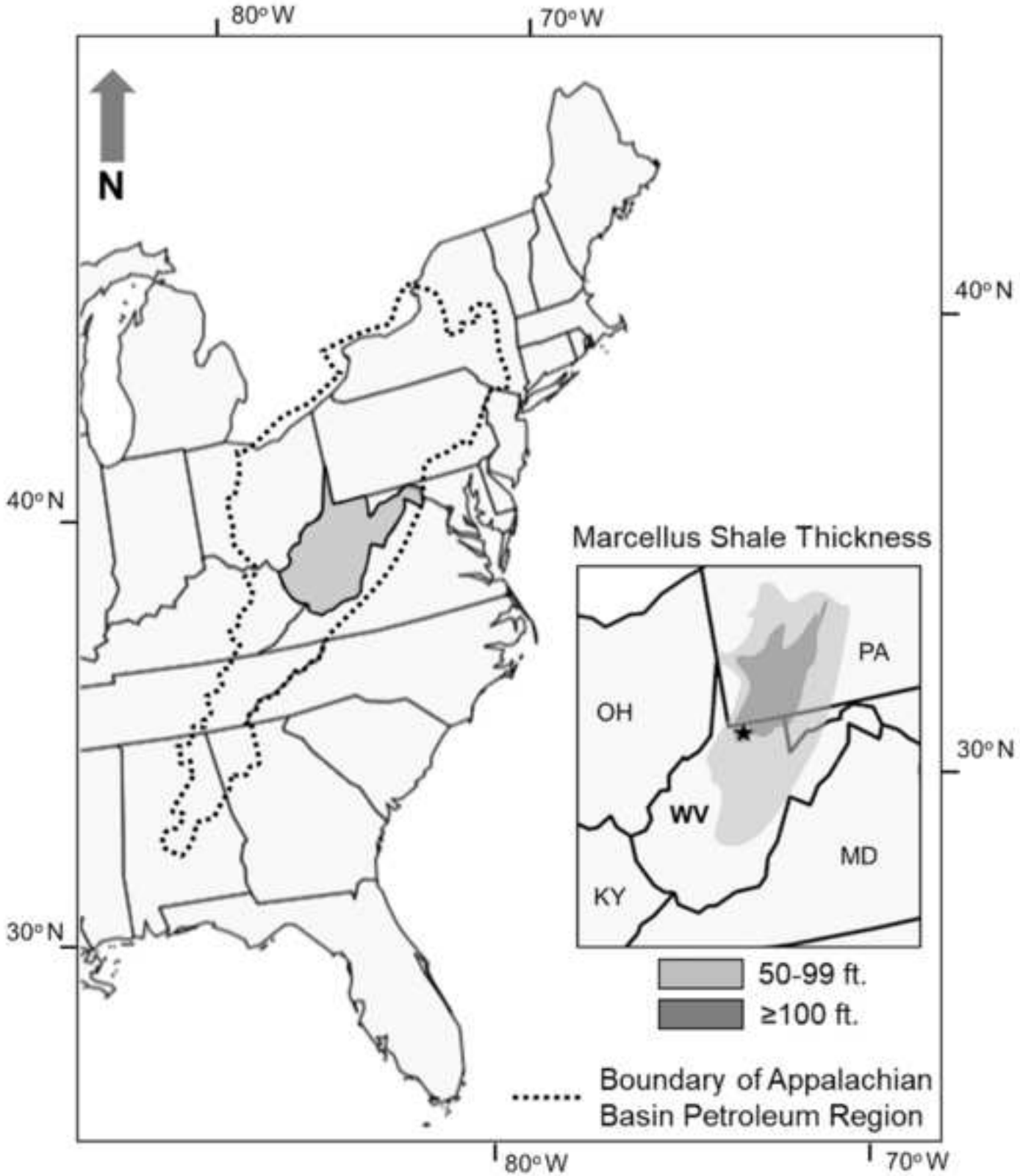

Figure 2
Click here to download high resolution image

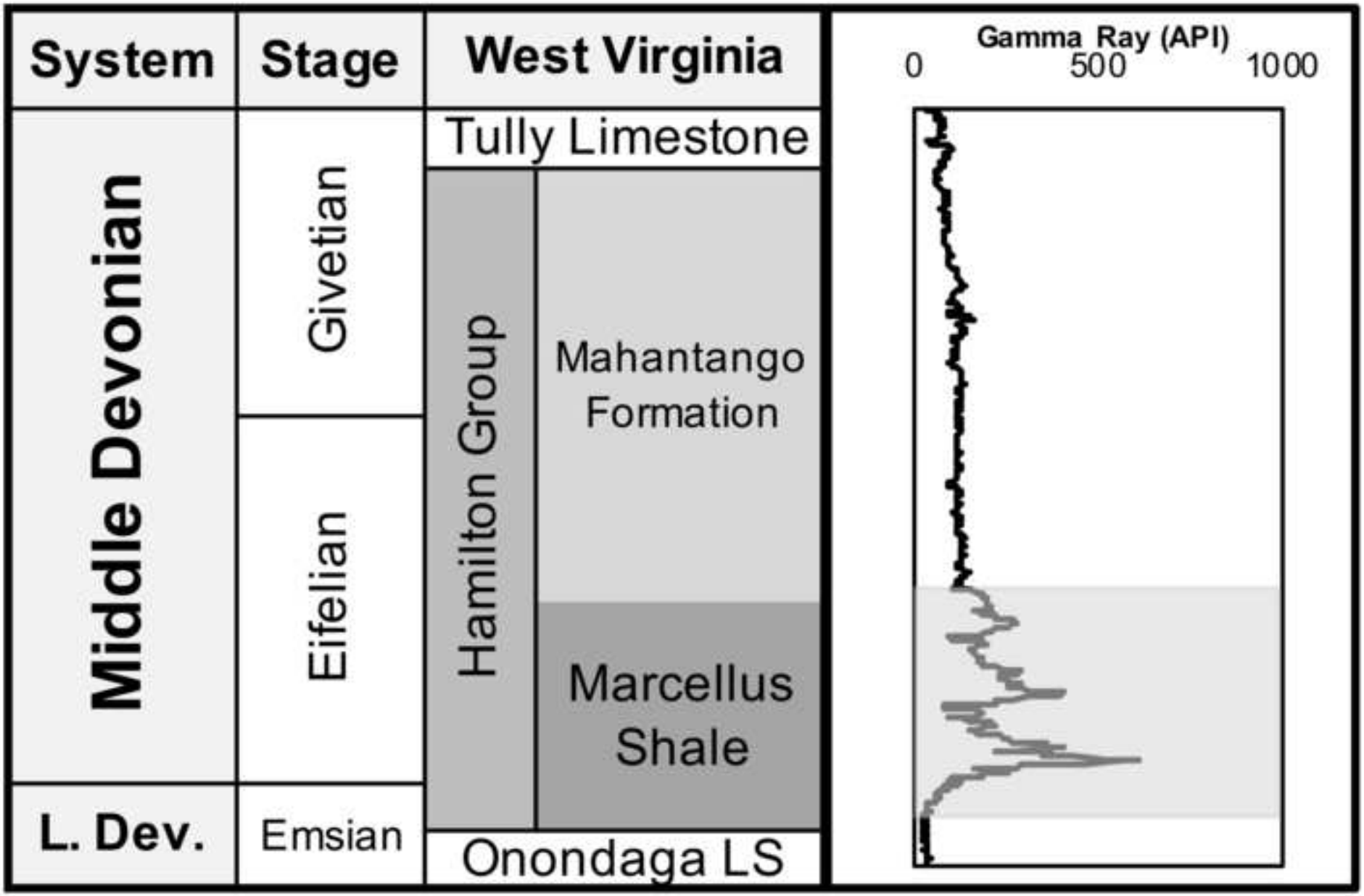

Figure 3
Click here to download high resolution image

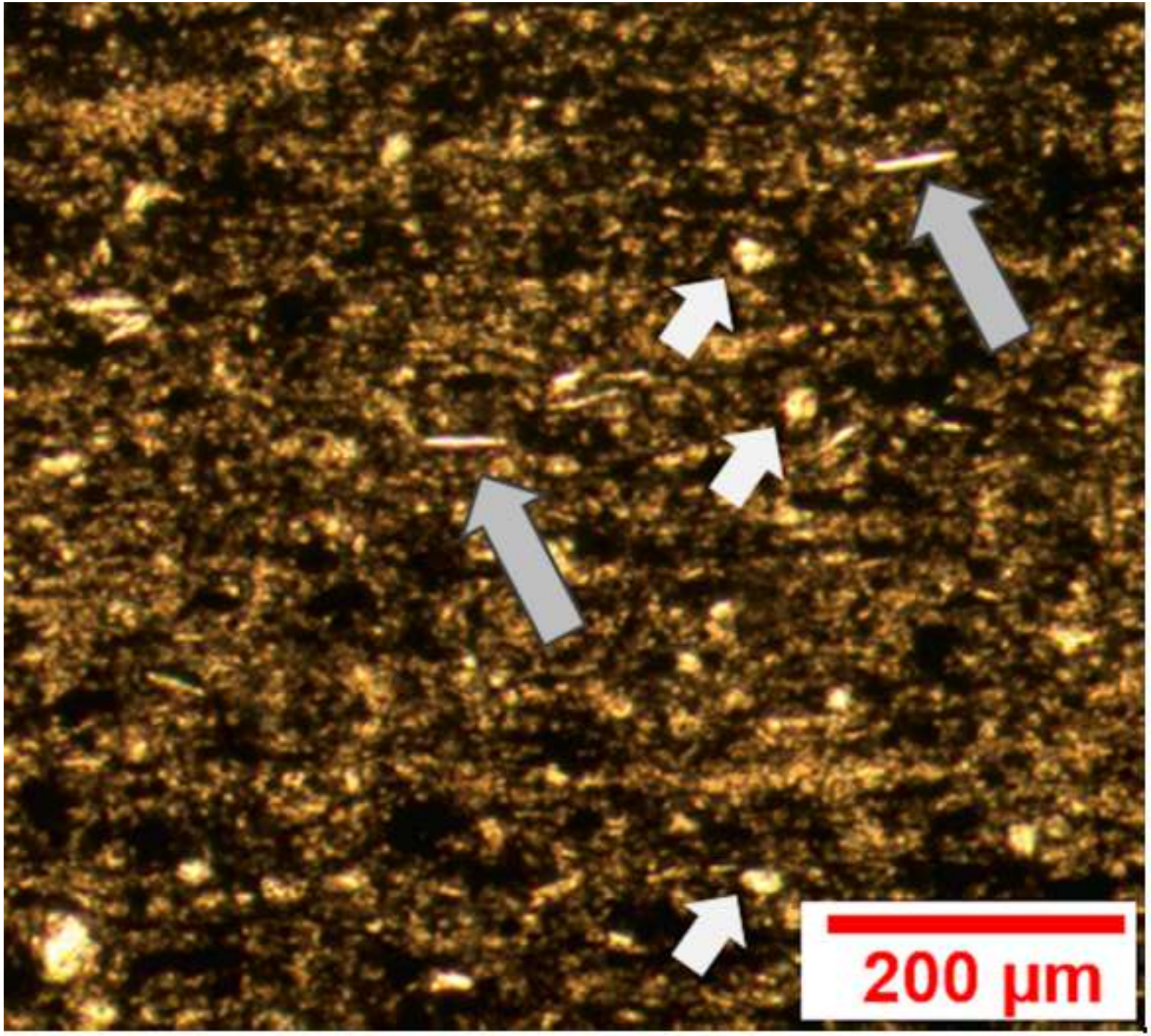

Figure 4
Click here to download high resolution image

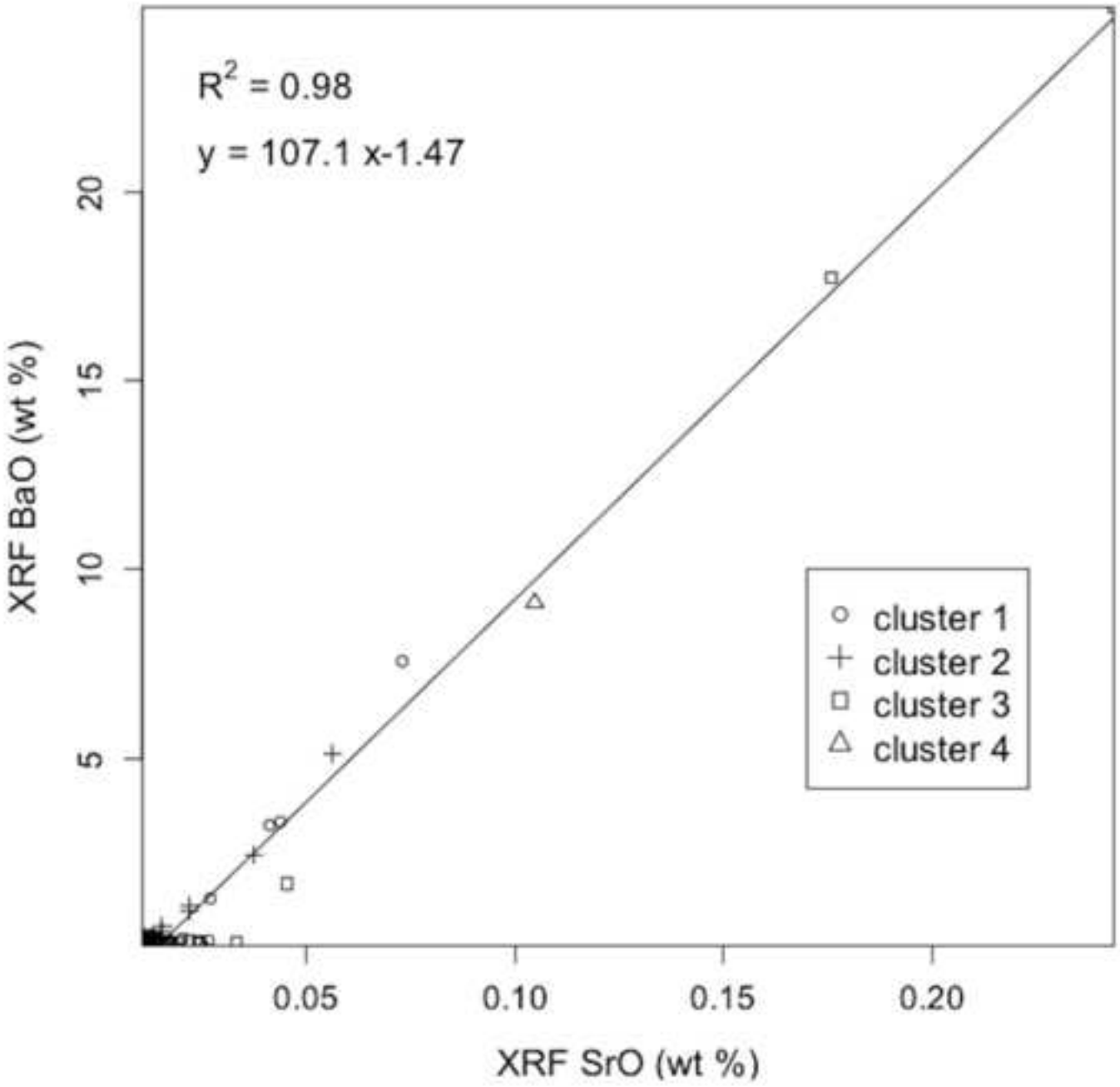

Figure 5
Click here to download high resolution image

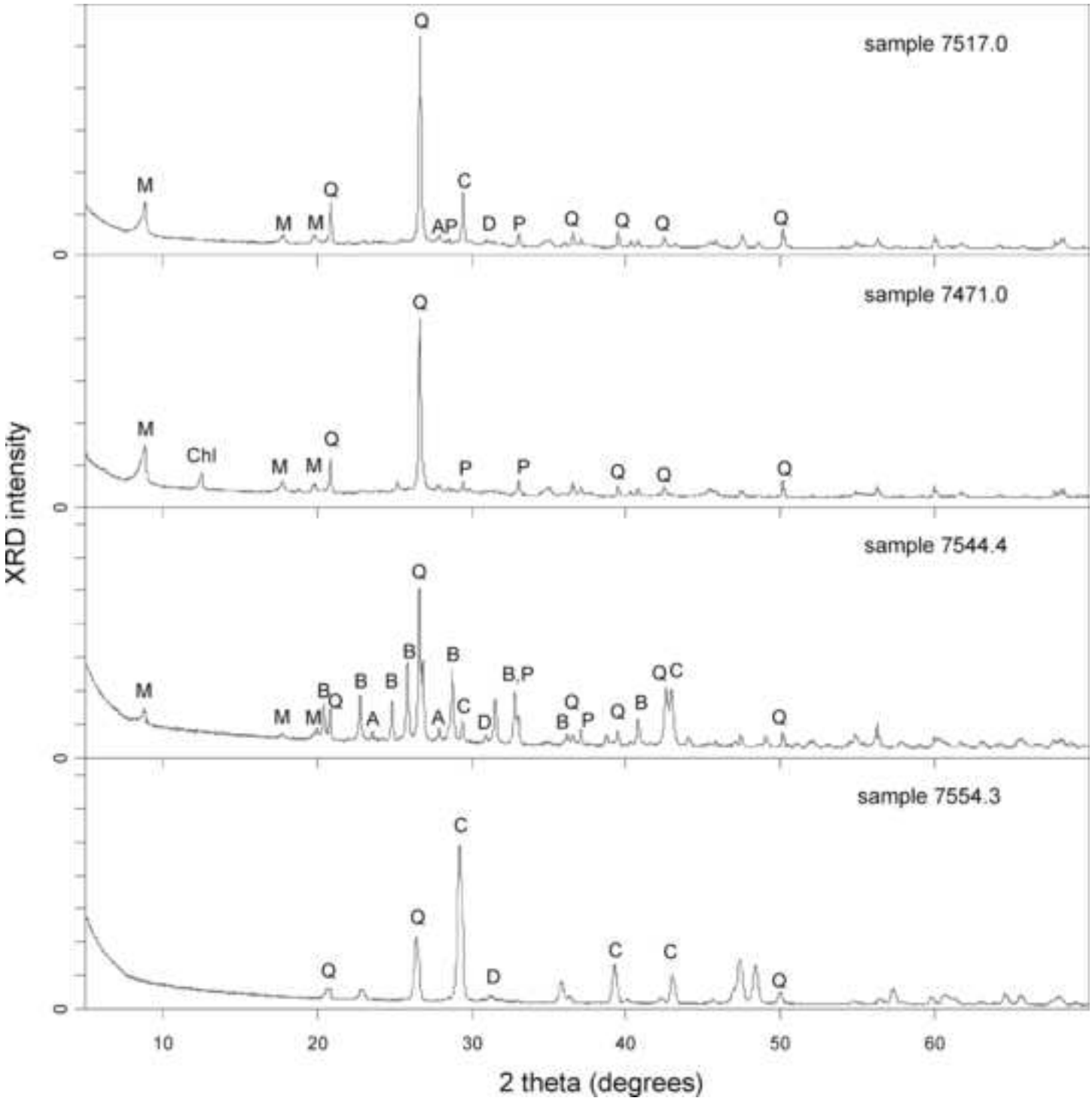

Figure 6
Click here to download high resolution image

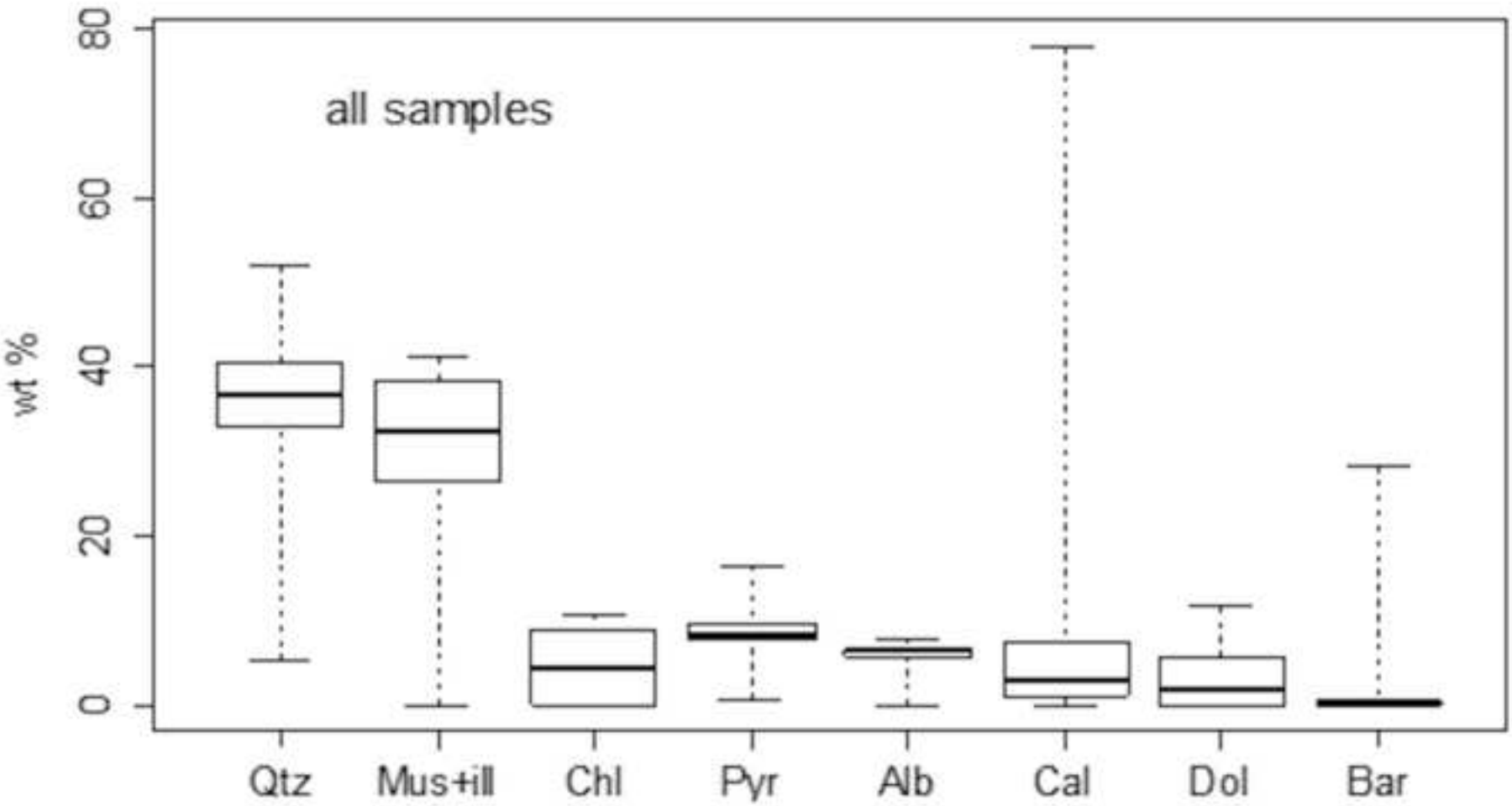

Figure 7
Click here to download high resolution image

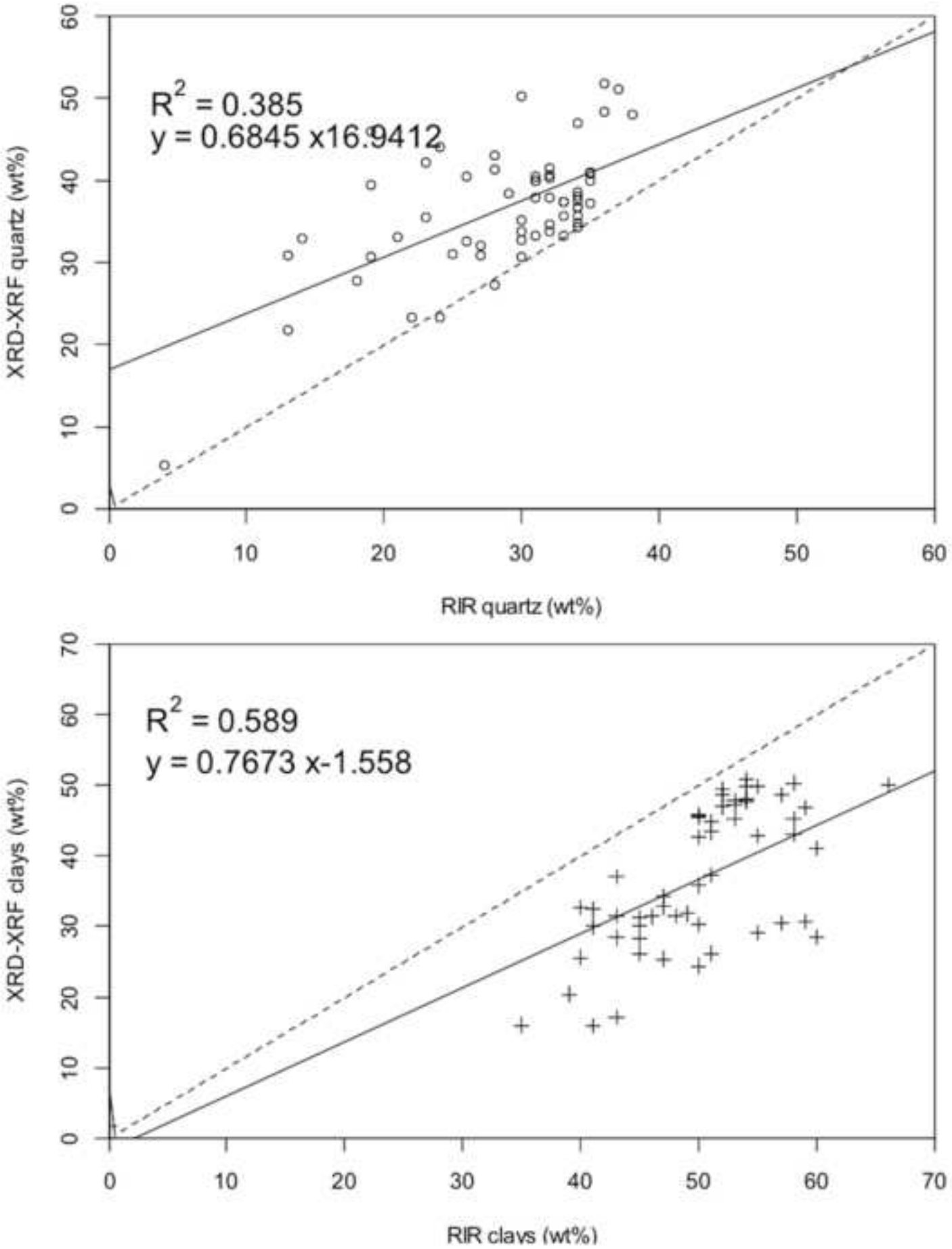

Figure 8
Click here to download high resolution image

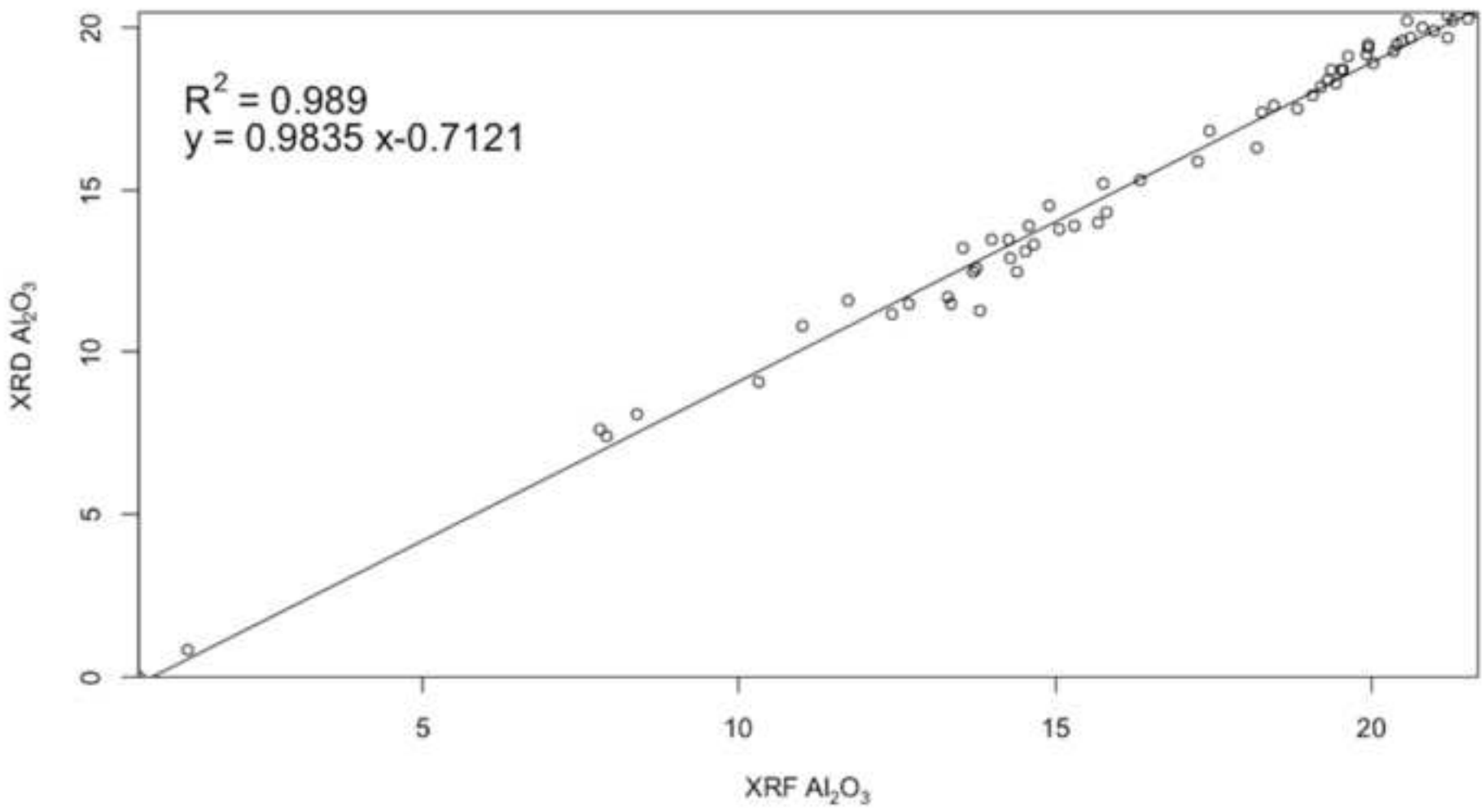

Figure 9
Click here to download high resolution image

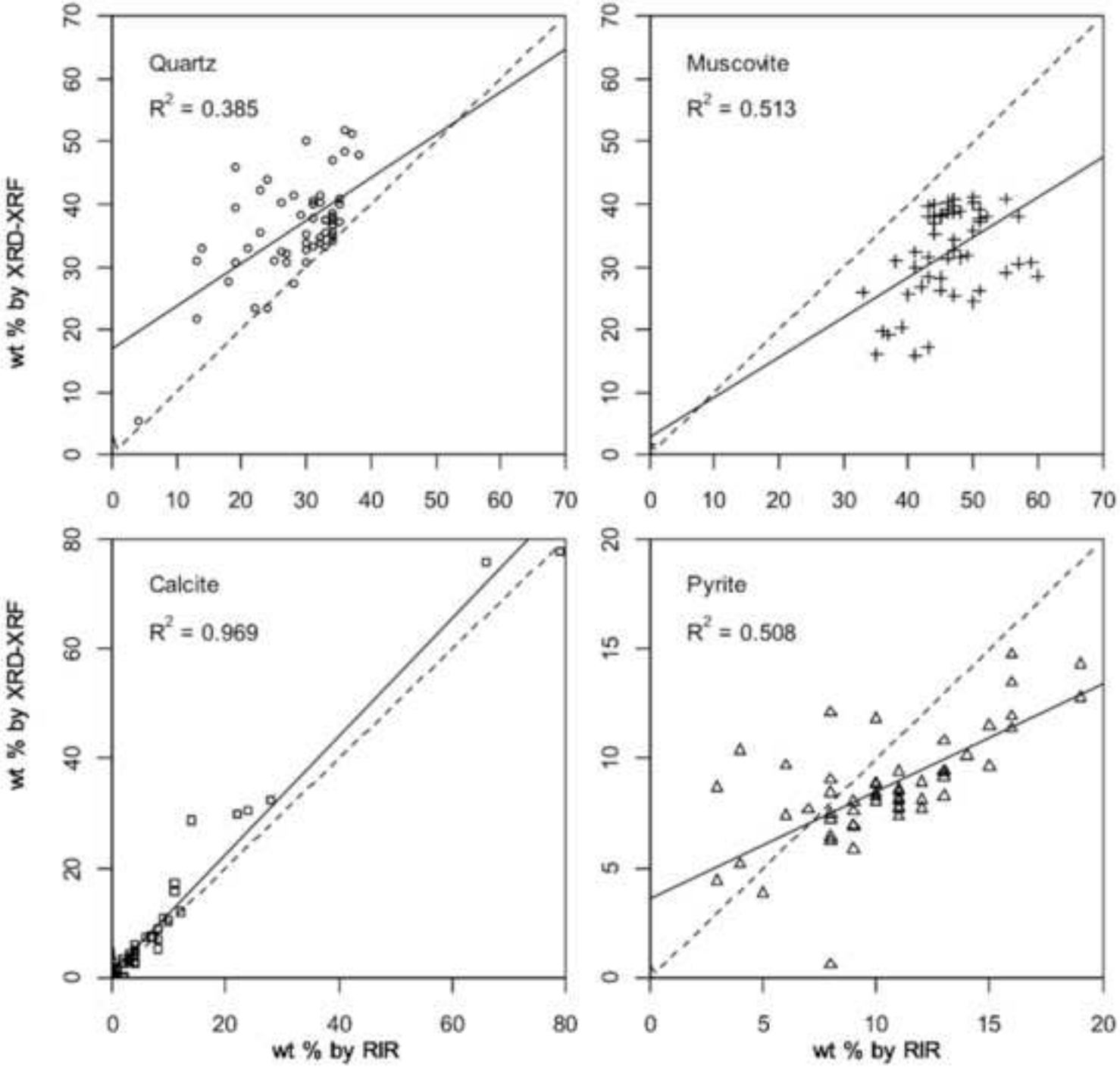

Figure 10
Click here to download high resolution image

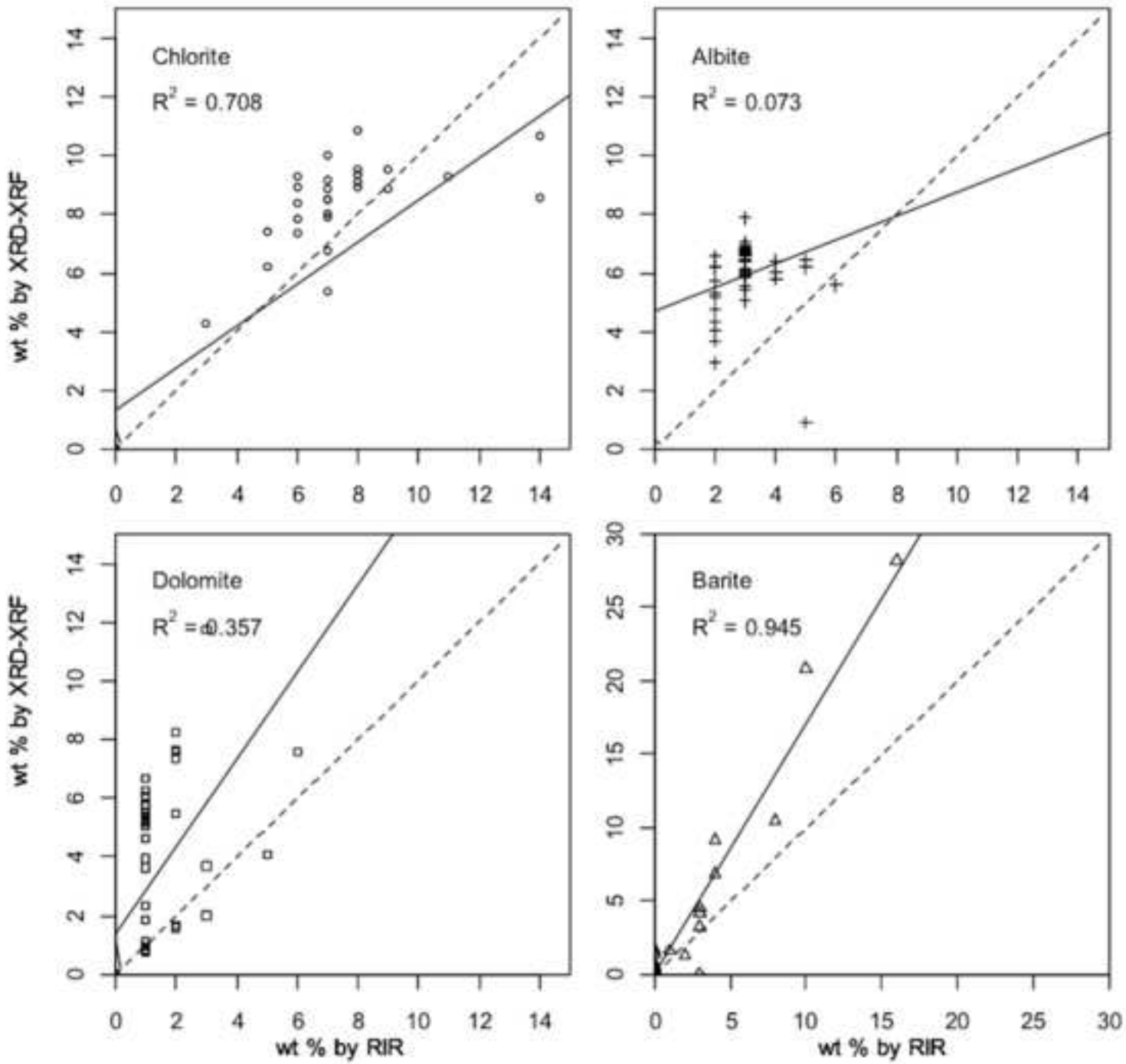

Figure 11
Click here to download high resolution image

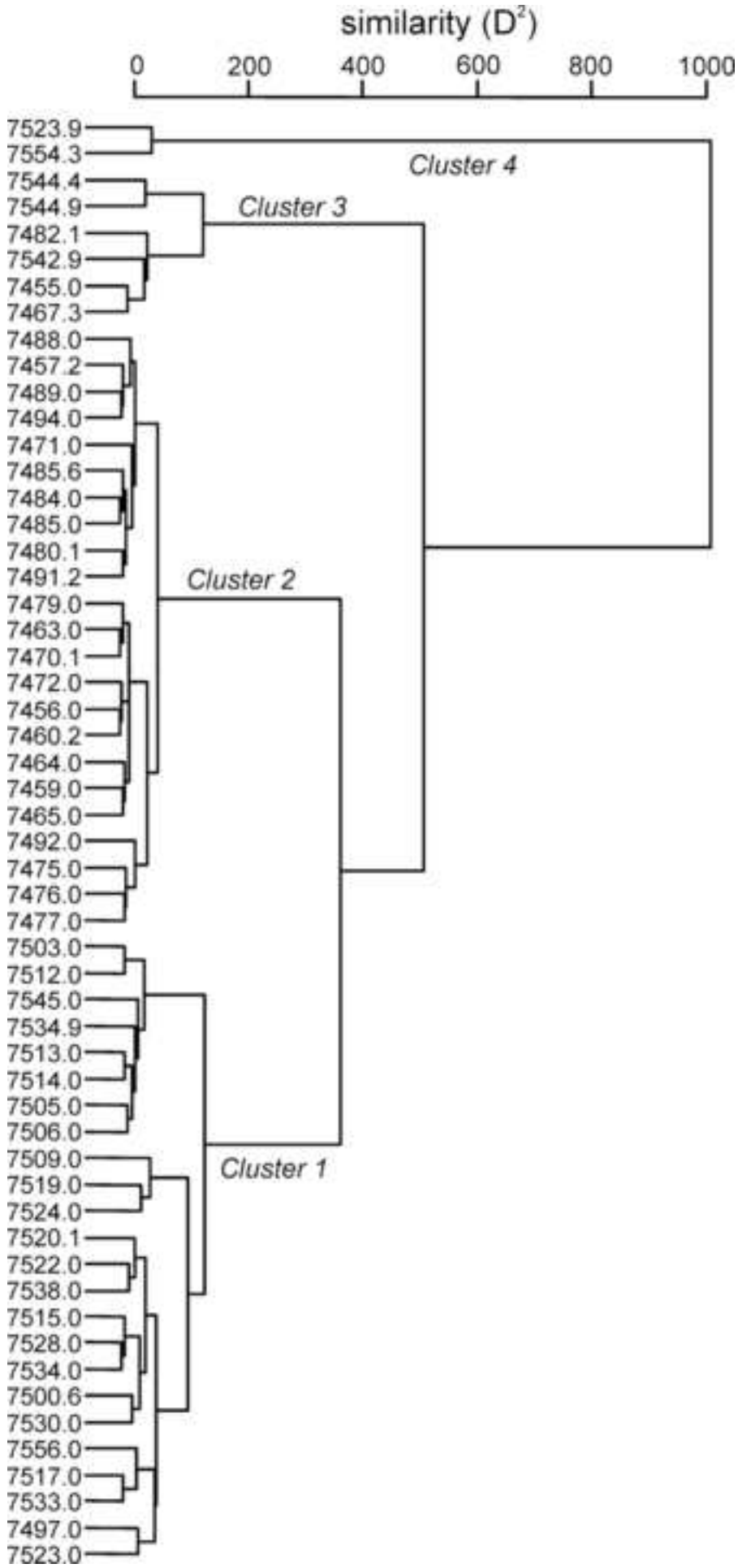

Figure 12-Color
Click here to download high resolution image

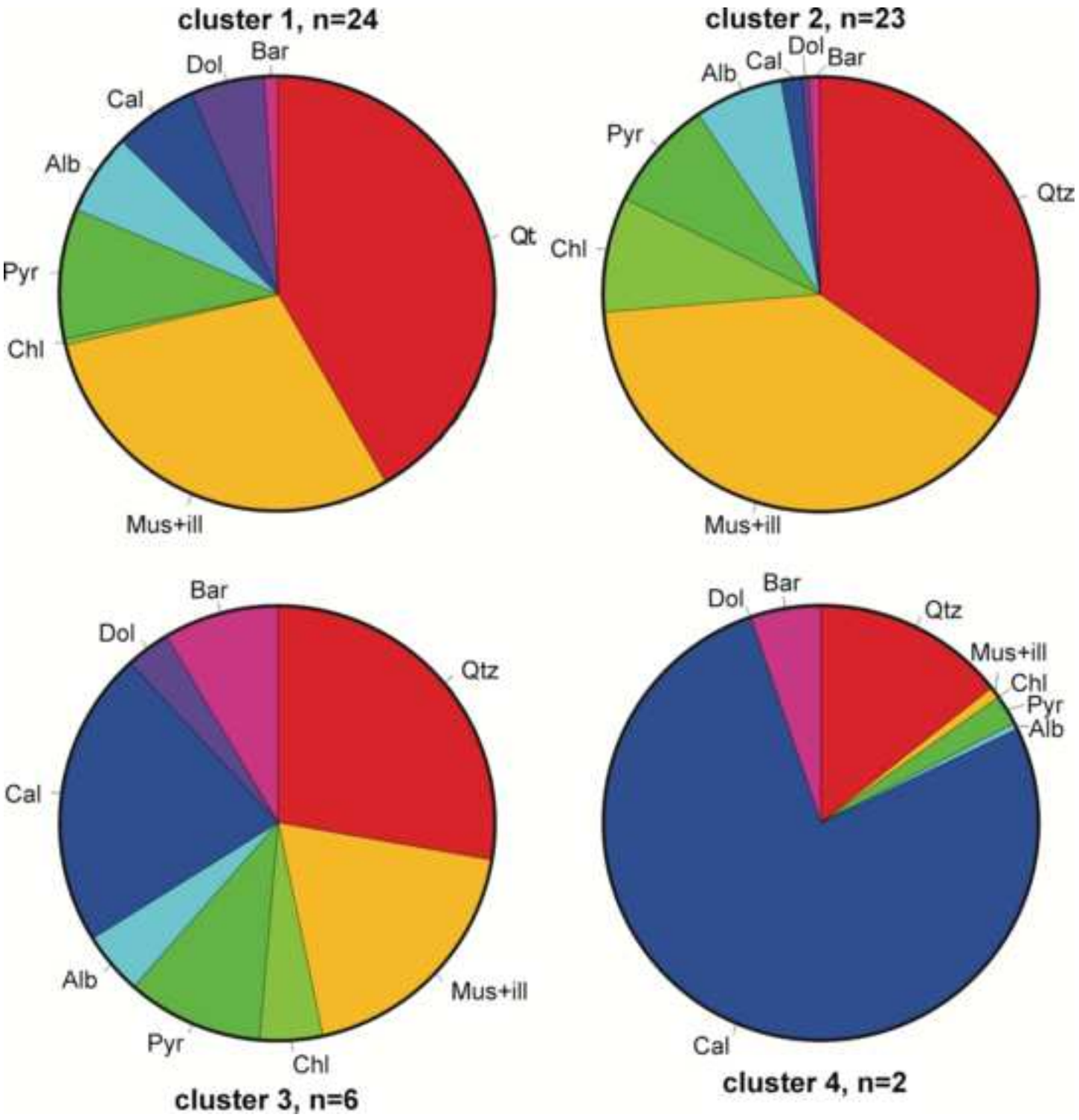

Figure 13
Click here to download high resolution image

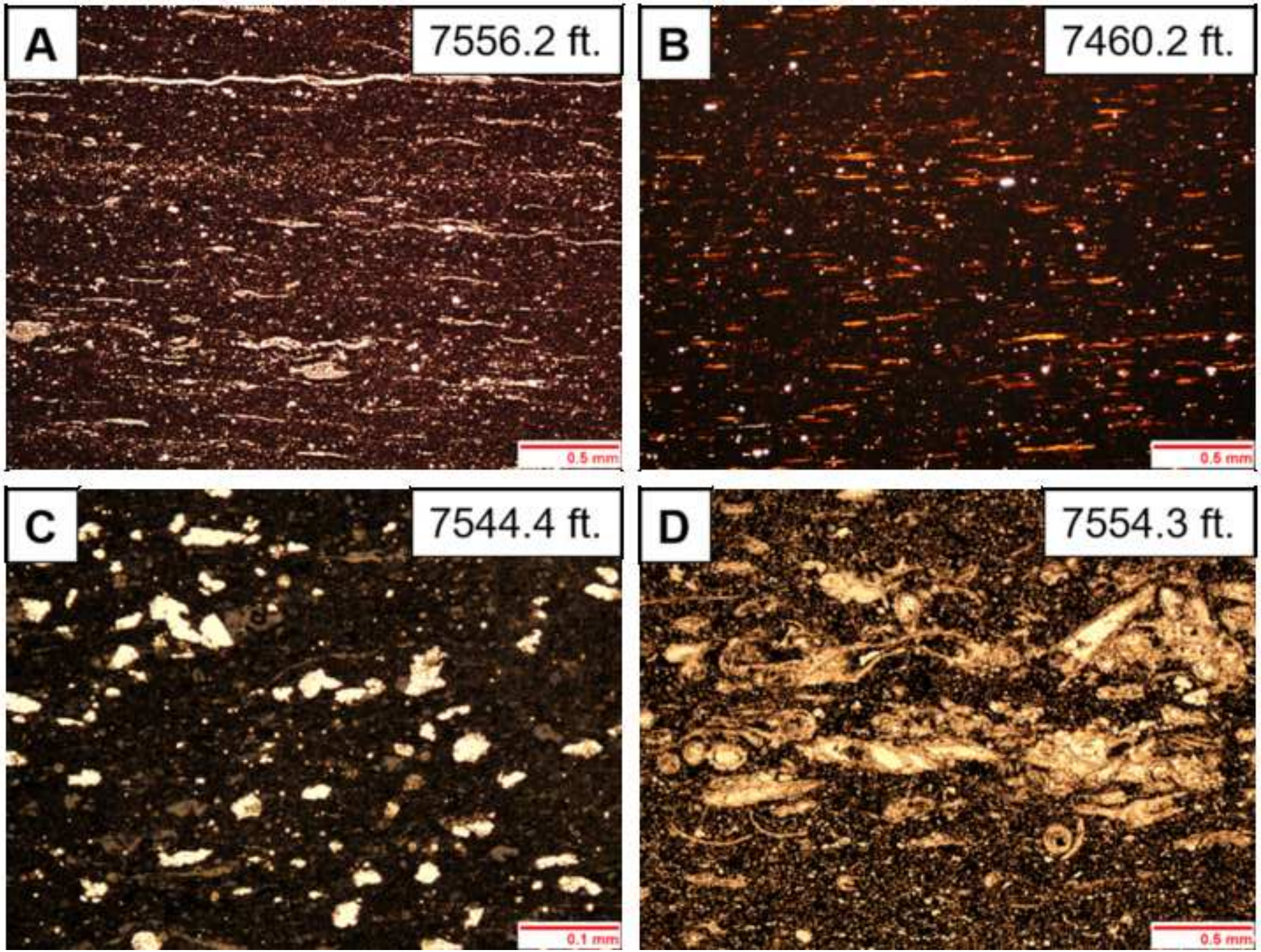

Figure 14

Click here to download high resolution image

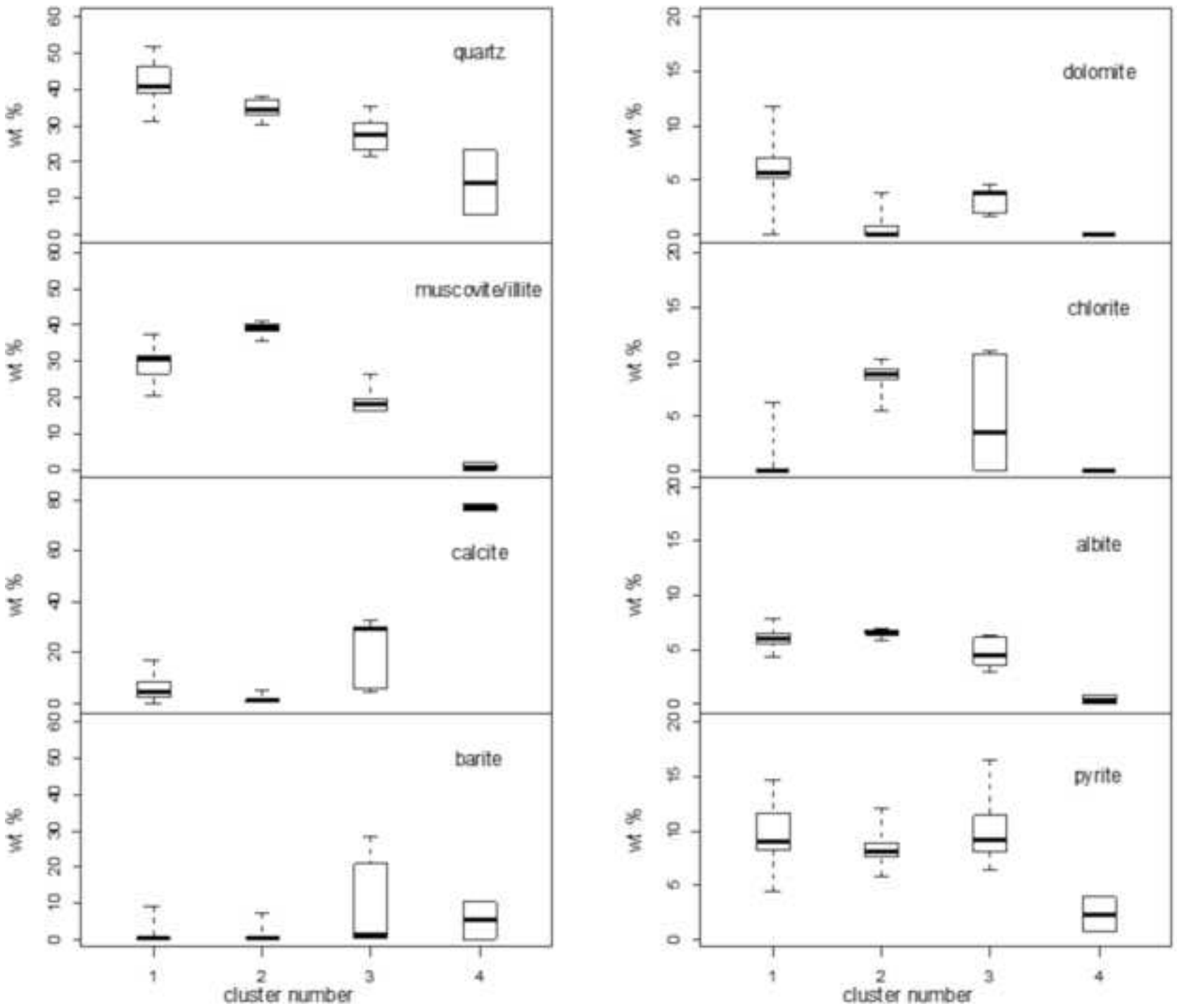

Figure 15
Click here to download high resolution image

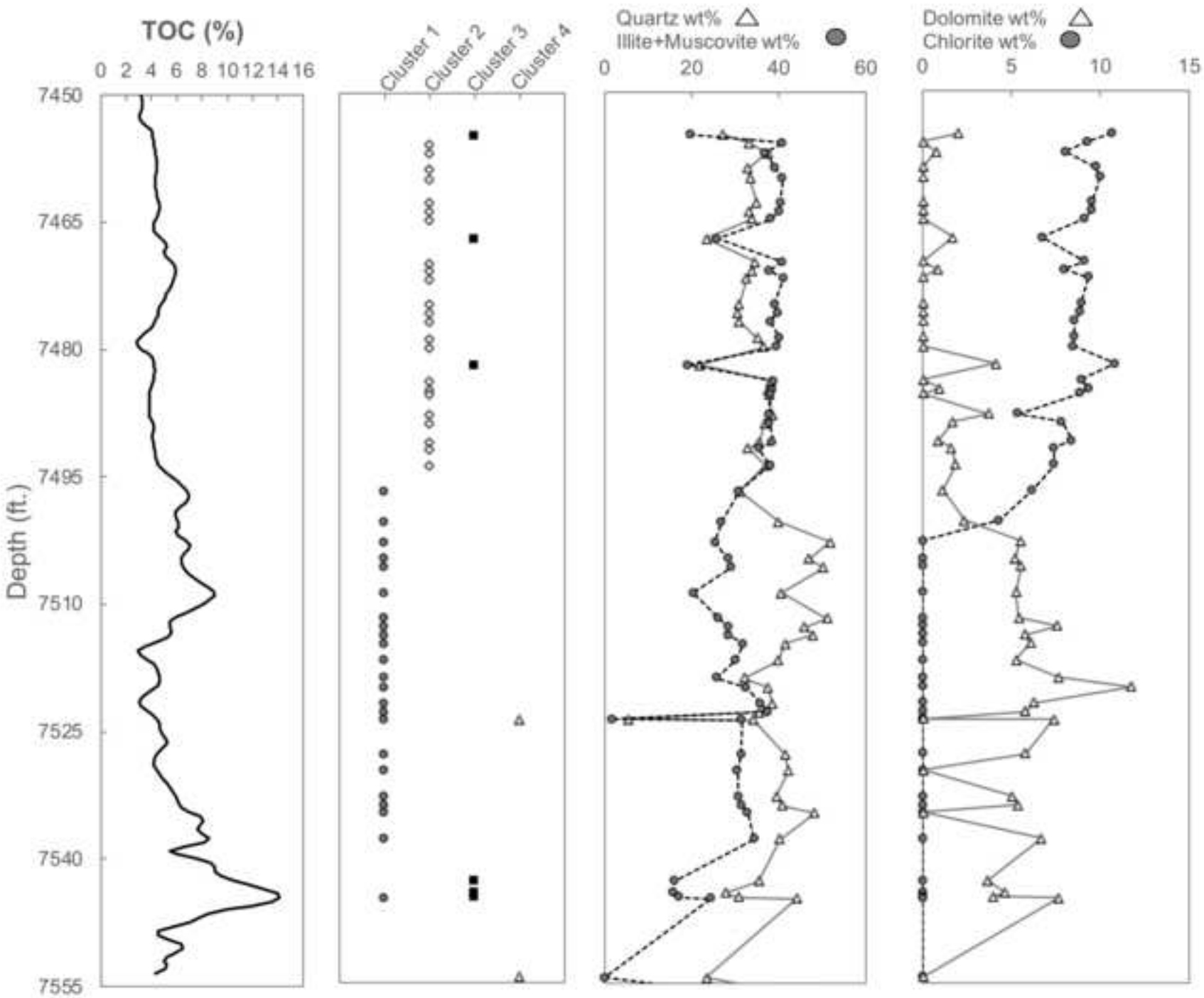

Table 1
Click here to download Table: Table 1_SedGeo.docx

Table 1.

Mineral Name	PDF2 Reference Code	Chemical Formula	Gram Formula wt.	RIR	Diagnostic Peak	I/I_o Intensity
Albite	00-009-0466	$NaAlSi_3O_8$	262.2	2.1	3.196 Å (002)	100
Barite	01-089-7357	$BaSO_4$	233.3	2.78	3.044 Å (021)	100
Calcite	01-083-0578	$CaCO_3$	100.0	3.21	3.035 Å (104)	100
Chlorite	01-089-2972	$Mg_{2.5}Fe_{1.65}Al_{1.5}Si_{2.2}Al_{1.8}O_{10}(OH)_8$	599.9	1.06	7.08 Å (001)	84.3
Dolomite	01-073-2409	$CaMg(CO_3)_2$	184.0	2.42	2.899 Å (104)	100
Muscovite	01-082-0576	$KAl_2(AlSi_3)O_{10}(OH)_2$	380.3	0.38	9.96 Å (001)	64.1
Pyrite	01-071-1680	FeS_2	119.9	0.89	2.708 Å (200)	100
Quartz	00-005-0490	SiO_2	60.1	3.6	3.34 Å (101)	100

Table 2

Click here to download Table: Table 2_SedGeo.docx

Sample (ft.)	Sample (m)	Quartz	Muscovite+ Illite	Chlorite	Pyrite	Albite	Calcite	Dolomite	Barite
7455.0	2272.3	28	36	14	3	2	14	3	0
7456.0	2272.6	21	55	11	10	3	0	0	0
7457.2	2272.9	33	44	7	13	2	0	1	0
7459.0	2273.5	14	51	27	4	5	0	0	0
7460.2	2273.9	31	47	7	11	3	0	0	0
7463.0	2274.7	34	46	9	8	3	0	0	0
7464.0	2275.0	33	44	8	11	3	0	0	0
7465.0	2275.3	30	45	8	14	3	0	0	0
7467.3	2276.0	24	33	7	10	2	22	2	0
7470.1	2276.9	32	47	7	12	3	0	0	0
7471.0	2277.2	32	43	7	11	2	2	1	2
7472.0	2277.5	26	50	8	13	3	0	0	0
7475.0	2278.4	27	46	8	12	3	2	0	3
7476.0	2278.7	30	43	9	13	2	4	0	0
7477.0	2279.0	13	57	14	8	4	4	0	0
7479.0	2279.6	30	50	7	9	3	1	0	0
7480.1	2279.9	34	47	7	9	3	1	0	0
7482.1	2280.6	13	37	8	8	2	28	5	0
7484.0	2281.1	34	48	6	8	3	0	0	0
7485.0	2281.4	34	47	6	9	3	0	1	0
7485.6	2281.6	31	52	7	8	3	0	0	0
7488.0	2282.3	29	51	7	7	3	1	3	0
7489.0	2282.6	34	44	6	11	2	0	2	0
7491.2	2283.3	33	46	6	11	3	1	1	0
7492.0	2283.6	30	44	6	10	3	1	2	4
7494.0	2284.2	35	45	5	9	3	1	1	0
7497.0	2285.1	25	38	5	19	2	8	1	1
7500.6	2286.2	31	42	3	10	3	7	1	3
7503.0	2286.9	36	47	0	10	2	3	2	0
7505.0	2287.5	34	45	0	16	3	1	1	0
7506.0	2287.8	30	55	0	8	3	2	1	0
7509.0	2288.7	31	39	0	16	2	11	1	0
7512.0	2289.7	37	45	0	13	3	1	1	0
7513.0	2290.0	19	60	0	6	6	4	6	0
7514.0	2290.3	38	43	0	13	2	3	1	0
7515.0	2290.6	28	49	0	11	3	8	1	0
7517.0	2291.2	35	41	0	11	3	9	1	0
7519.0	2291.8	27	40	0	19	3	6	2	4
7520.1	2292.1	33	41	0	9	3	3	3	0
7522.0	2292.7	34	50	0	8	3	4	1	0
7523.0	2293.0	34	51	0	4	3	8	1	0
7523.9	2293.3	4	0	0	5	5	79	0	8
7524.0	2293.3	34	48	0	3	3	11	2	0
7528.0	2294.5	32	46	0	11	3	8	1	0
7530.0	2295.1	23	57	0	10	4	3	0	3
7533.0	2296.1	19	59	0	10	4	10	1	0
7534.0	2296.4	35	43	0	12	3	7	1	0
7534.9	2296.6	36	47	0	11	3	3	0	0
7538.0	2297.6	32	47	0	15	3	2	1	0
7542.9	2299.1	23	35	0	15	2	24	1	0
7544.4	2299.5	18	41	0	16	5	4	1	16
7544.9	2299.7	19	43	0	21	3	4	1	10
7545.0	2299.7	24	50	0	16	3	4	2	0
7554.3	2302.6	22	0	0	8	0	66	0	3
7556.0	2303.1	26	51	0	6	3	12	2	0

Table 3

Click here to download Table: Table 3_SedGeo.docx

Sample (ft.)	Sample (m)	SiO_2	Al_2O_3	FeO	MgO	CaO	Na_2O	K_2O	SO_3	BaO	SrO	LOI 600°C	LOI 900°C
7455.0	2272.3	43.9	13.3	7.33	2.39	17.93	0.37	2.61	1.90	0.109	0.024	4.13	9.39
7456.0	2272.6	60.4	21.5	6.87	1.60	0.55	0.82	5.17	0.41	0.213	0.013	9.78	2.12
7457.2	2272.9	62.9	19.4	7.06	1.56	0.62	0.80	4.70	0.35	0.272	0.013	8.49	2.01
7459.0	2273.5	60.2	21.2	7.99	1.69	0.59	0.79	5.03	0.16	0.218	0.012	10.97	1.93
7460.2	2273.9	60.7	21.7	6.77	1.72	0.38	0.78	5.18	0.48	0.201	0.013	10.76	1.85
7463.0	2274.7	62.0	21.3	5.93	1.64	0.48	0.80	5.12	0.37	0.409	0.015	8.04	1.77
7464.0	2275.0	59.7	20.8	6.20	1.63	1.68	0.77	5.05	0.85	0.208	0.014	8.16	2.77
7465.0	2275.3	60.5	20.3	7.74	1.59	0.74	0.83	4.90	0.50	0.542	0.015	10.08	2.06
7467.3	2276.0	42.6	14.5	6.24	1.60	18.41	0.51	3.42	3.36	0.159	0.022	7.46	8.43
7470.1	2276.9	59.4	20.5	5.91	1.51	0.52	0.78	4.95	0.24	0.184	0.012	14.38	5.54
7471.0	2277.2	59.2	19.5	6.53	1.55	2.24	0.75	4.81	1.43	0.972	0.022	9.42	2.66
7472.0	2277.5	60.1	21.2	6.55	1.61	0.49	0.80	5.21	0.58	1.092	0.022	10.88	2.01
7475.0	2278.4	57.2	20.4	6.89	1.54	1.53	0.78	4.97	1.23	2.438	0.037	10.34	2.59
7476.0	2278.7	57.3	20.5	7.06	1.54	2.98	0.75	5.06	1.69	0.201	0.013	9.02	2.62
7477.0	2279.0	57.1	20.0	8.90	1.50	2.49	0.71	4.90	1.45	0.171	0.015	9.29	2.49
7479.0	2279.6	62.0	21.0	5.99	1.46	0.85	0.83	5.09	0.50	0.194	0.010	8.98	1.77
7480.1	2279.9	63.3	20.6	5.55	1.46	0.69	0.83	5.01	0.39	0.249	0.011	7.81	1.72
7482.1	2280.6	45.1	12.7	6.94	2.29	24.42	0.55	2.99	1.20	1.680	0.045	10.53	1.67
7484.0	2281.1	64.7	19.9	5.23	1.54	0.51	0.82	4.93	0.28	0.190	0.011	9.13	1.63
7485.0	2281.4	64.6	19.9	5.10	1.62	0.63	0.84	4.94	0.34	0.190	0.011	8.77	1.58
7485.6	2281.6	64.4	19.6	6.04	1.54	0.54	0.81	4.86	0.25	0.197	0.011	8.21	1.58
7488.0	2282.3	63.4	19.0	5.56	1.76	1.44	0.78	4.79	0.92	0.193	0.011	8.00	1.85
7489.0	2282.6	62.6	19.5	6.21	1.73	1.12	0.80	4.83	0.57	0.178	0.011	7.62	2.15
7491.2	2283.3	62.3	19.9	6.14	1.64	1.11	0.84	4.92	0.42	0.210	0.012	8.60	2.21
7492.0	2283.6	58.3	18.8	6.47	1.67	1.29	0.79	4.59	0.38	5.121	0.056	10.67	2.31
7494.0	2284.2	62.8	19.3	5.44	1.69	1.61	0.81	4.82	0.60	0.173	0.012	8.91	2.41
7497.0	2285.1	55.1	16.3	10.27	1.39	5.81	0.73	4.13	3.05	1.275	0.027	9.84	1.70
7500.6	2286.2	60.5	13.5	6.23	1.29	5.15	0.75	3.49	3.19	3.220	0.041	9.97	2.33
7503.0	2286.9	68.4	12.4	5.41	1.22	3.52	0.62	3.19	1.37	0.116	0.013	10.14	3.23
7505.0	2287.5	67.5	14.4	8.46	1.20	1.14	0.73	3.68	0.51	0.141	0.011	11.20	2.00
7506.0	2287.8	69.5	14.3	5.53	1.23	1.76	0.71	3.69	0.97	0.133	0.012	11.67	1.90
7509.0	2288.7	57.4	10.3	7.72	1.24	12.24	0.56	2.73	5.21	0.124	0.018	8.97	2.27
7512.0	2289.7	69.1	13.3	6.62	1.21	1.86	0.72	3.32	0.21	0.154	0.012	14.00	2.98
7513.0	2290.0	64.3	13.8	5.89	1.69	3.82	0.67	3.59	1.76	0.142	0.014	13.81	3.69
7514.0	2290.3	65.9	13.7	5.73	1.28	3.42	0.64	3.57	1.11	0.129	0.014	11.46	3.86
7515.0	2290.6	62.9	15.7	5.85	1.38	4.98	0.73	4.10	2.52	0.135	0.017	10.76	1.49
7517.0	2291.2	60.7	14.7	4.56	1.19	8.03	0.79	3.85	3.50	0.137	0.024	9.61	2.26
7519.0	2291.8	53.1	13.8	8.50	1.85	7.14	0.71	3.51	0.74	7.569	0.073	11.47	2.60
7520.1	2292.1	59.6	15.8	5.00	2.67	5.79	0.82	4.17	2.61	0.161	0.014	11.97	2.93
7522.0	2292.7	61.6	17.2	5.13	1.39	3.56	0.94	4.48	1.31	0.206	0.014	10.83	3.58
7523.0	2293.0	60.5	18.2	3.25	1.32	7.09	0.83	4.82	2.23	0.224	0.020	10.20	1.39
7523.9	2293.3	7.8	1.3	2.68	0.70	50.56	0.12	0.24	0.13	9.129	0.105	10.02	23.35
7524.0	2293.3	55.4	15.3	2.74	1.67	11.51	0.79	4.04	2.25	0.195	0.027	7.54	5.44
7528.0	2294.5	62.1	15.1	5.03	1.29	5.79	0.74	3.99	0.38	0.139	0.016	10.77	4.85
7530.0	2295.1	61.5	14.0	7.14	1.06	2.52	0.76	3.81	1.12	3.328	0.044	8.98	4.26
7533.0	2296.1	59.6	14.2	5.07	1.13	7.54	0.73	3.90	2.20	0.141	0.019	8.27	4.98
7534.0	2296.4	61.0	14.6	4.94	1.19	5.84	0.79	3.95	1.20	0.190	0.017	7.64	5.70
7534.9	2296.6	67.9	14.9	4.83	1.15	2.13	0.79	4.02	0.68	0.129	0.012	9.53	3.05
7538.0	2297.6	61.3	15.8	6.89	1.46	1.91	0.83	4.25	0.63	0.162	0.012	19.48	5.90
7542.9	2299.1	49.8	7.9	6.22	0.86	19.54	0.61	2.13	2.45	0.107	0.033	9.84	8.74
7544.4	2299.5	41.5	7.8	7.16	1.06	4.99	0.77	2.07	2.40	24.913	0.244	9.01	5.46
7544.9	2299.7	45.5	8.4	10.46	0.91	4.06	0.77	2.24	1.99	17.751	0.176	11.03	6.28
7545.0	2299.7	60.8	11.0	9.10	1.73	4.69	0.62	3.11	1.28	0.164	0.016	16.29	6.13
7554.3	2302.6	22.5	0.5	0.35	0.42	40.87	0.04	0.07	0.20	0.013	0.025	3.34	30.39
7556.0	2303.1	60.0	11.7	4.70	1.92	9.79	0.70	3.43	2.72	0.120	0.024	12.12	4.19

Table 4

Click here to download Table: Table 4_SedGeo.docx

Sample (ft.)	Sample (m)	Quartz	Musc..+Ill.	Chlorite	Pyrite	Albite	Calcite	Dolomite	Barite	Normalization Factor	Cluster
7455.0	2272.3	27.2	19.6	10.66	8.66	2.94	28.7	2.01	0.19	0.939	3
7456.0	2272.6	33.0	40.8	9.30	8.82	6.79	0.97	0.00	0.30	0.987	2
7457.2	2272.9	37.4	36.8	8.04	9.37	6.55	0.67	0.76	0.38	0.980	2
7459.0	2273.5	32.9	39.2	9.73	10.37	6.43	1.01	0.00	0.30	0.954	2
7460.2	2273.9	33.3	40.8	10.01	8.46	6.42	0.66	0.00	0.28	0.965	2
7463.0	2274.7	34.8	40.4	9.53	7.22	6.63	0.84	0.00	0.58	0.987	2
7464.0	2275.0	33.2	40.0	9.54	7.70	6.39	2.94	0.00	0.30	0.990	2
7465.0	2275.3	33.7	38.2	9.14	10.14	6.77	1.27	0.00	0.73	0.976	2
7467.3	2276.0	23.4	25.9	6.75	8.03	4.04	29.9	1.68	0.25	0.945	3
7470.1	2276.9	34.6	40.7	9.15	7.69	6.68	0.95	0.00	0.27	0.966	2
7471.0	2277.2	33.8	37.9	7.93	8.60	6.21	3.46	0.81	1.31	0.984	2
7472.0	2277.5	32.5	41.0	9.35	8.25	6.61	0.84	0.00	1.44	0.983	2
7475.0	2278.4	30.8	39.0	8.90	8.90	6.44	2.65	0.00	3.24	0.985	2
7476.0	2278.7	30.6	39.7	8.89	9.16	6.19	5.16	0.00	0.29	0.980	2
7477.0	2279.0	30.9	38.1	8.58	12.06	5.80	4.27	0.00	0.25	0.970	2
7479.0	2279.6	35.1	40.2	8.51	7.59	6.84	1.49	0.00	0.27	0.988	2
7480.1	2279.9	36.6	39.6	8.49	6.88	6.87	1.20	0.00	0.35	0.989	2
7482.1	2280.6	21.8	19.2	10.85	6.41	3.68	32.4	4.09	1.63	0.783	3
7484.0	2281.1	38.1	38.8	8.93	6.21	6.79	0.89	0.00	0.27	0.984	2
7485.0	2281.4	37.5	38.6	9.32	5.85	6.89	0.57	0.94	0.27	0.978	2
7485.6	2281.6	37.8	38.0	8.85	7.49	6.62	0.94	0.00	0.28	0.977	2
7488.0	2282.3	38.4	37.7	5.38	7.65	6.41	0.49	3.70	0.28	0.983	2
7489.0	2282.6	36.7	37.9	7.83	8.06	6.55	1.02	1.68	0.26	0.981	2
7491.2	2283.3	35.6	38.6	8.38	7.81	6.92	1.46	0.85	0.30	0.981	2
7492.0	2283.6	32.8	35.3	7.39	8.41	6.40	1.33	1.60	6.73	0.938	2
7494.0	2284.2	37.1	38.0	7.41	6.95	6.67	1.78	1.87	0.25	0.985	2
7497.0	2285.1	31.1	30.9	6.20	14.30	5.70	9.00	1.12	1.63	0.935	1
7500.6	2286.2	39.9	26.9	4.30	8.81	6.02	7.49	2.34	4.27	0.961	1
7503.0	2286.9	51.7	25.4	0.00	8.87	5.19	3.19	5.48	0.18	0.990	1
7505.0	2287.5	46.9	28.3	0.00	13.45	5.91	0.00	5.21	0.20	0.961	1
7506.0	2287.8	50.2	29.1	0.00	9.03	5.86	0.07	5.52	0.19	0.986	1
7509.0	2288.7	40.5	20.4	0.00	11.93	4.36	17.4	5.25	0.19	0.933	1
7512.0	2289.7	51.1	26.2	0.00	10.81	6.00	0.31	5.40	0.21	0.952	1
7513.0	2290.0	45.9	28.5	0.00	9.67	5.59	2.59	7.58	0.20	0.991	1
7514.0	2290.3	47.9	28.4	0.00	9.43	5.34	2.88	5.78	0.19	0.995	1
7515.0	2290.6	41.3	31.8	0.00	9.38	5.91	5.24	6.07	0.20	0.971	1
7517.0	2291.2	39.9	30.0	0.00	7.33	6.44	11.0	5.23	0.22	0.971	1
7519.0	2291.8	32.1	25.6	0.00	12.81	5.45	7.37	7.62	8.97	0.884	1
7520.1	2292.1	37.4	32.4	0.00	8.02	6.70	3.56	11.74	0.23	0.971	1
7522.0	2292.7	38.5	35.8	0.00	8.45	7.89	2.86	6.26	0.29	0.998	1
7523.0	2293.0	35.6	37.3	0.00	5.19	6.75	8.97	5.79	0.32	0.969	1
7523.9	2293.3	5.3	1.6	0.00	3.81	0.90	75.3	2.72	10.34	0.854	4
7524.0	2293.3	34.2	31.5	0.00	4.41	6.43	15.8	7.37	0.31	0.975	1
7528.0	2294.5	41.4	31.4	0.00	8.17	6.09	6.94	5.76	0.20	0.929	1
7530.0	2295.1	41.3	29.9	0.00	11.56	6.28	1.81	4.69	4.53	0.979	1
7533.0	2296.1	39.4	30.7	0.00	8.24	6.03	10.4	5.04	0.23	0.982	1
7534.0	2296.4	40.8	31.5	0.00	8.13	6.56	7.37	5.37	0.29	0.995	1
7534.9	2296.6	47.2	32.0	0.00	7.94	6.58	0.93	5.18	0.19	0.993	1
7538.0	2297.6	40.2	34.3	0.00	11.50	7.06	0.00	6.66	0.22	0.940	1
7542.9	2299.1	35.4	16.0	0.00	9.64	4.77	30.4	3.64	0.18	0.933	3
7544.4	2299.5	27.7	15.9	0.00	11.36	6.21	5.95	4.61	28.28	0.955	3
7544.9	2299.7	30.7	17.1	0.00	16.50	6.14	4.71	3.93	20.94	0.950	3
7545.0	2299.7	44.0	24.4	0.00	14.73	5.05	3.96	7.65	0.22	0.977	1
7554.3	2302.6	23.2	0.0	0.00	0.60	0.00	74.1	1.99	0.06	1.036	4
7556.0	2303.1	40.4	26.2	0.00	7.40	5.57	12.0	8.26	0.19	0.951	1

Table 5

Click here to download Table: Table 5_SedGeo.docx

Mineral	Cluster 1 (n=24)		Cluster 2 (n=23)		Cluster 3 (n=6)		Cluster 4 (n=2)	
Phase	Avg.	±	Avg.	±	Avg.	±	Avg.	±
Qtz	41.62	5.60	34.67	2.43	27.69	4.92	14.24	12.68
Musc+Ill	29.54	3.80	38.94	1.42	18.96	3.76	0.82	1.16
Chl	0.44	1.51	8.64	1.01	4.71	5.36	0.00	0.00
Pyr	9.57	2.63	8.24	1.39	10.10	3.54	2.20	2.27
Alb	6.03	0.73	6.56	0.27	4.63	1.33	0.45	0.63
Cal	5.88	4.94	1.60	1.25	22.00	12.98	74.73	0.84
Dol	5.93	2.00	0.53	0.93	3.33	1.19	2.36	0.52
Bar	1.00	2.08	0.82	1.45	8.58	12.64	5.20	7.26